Biophysical Journal
Article

Biophysical Society

NMR Structural Analysis of Isolated *Shaker* Voltage-Sensing Domain in LPPG Micelles

Hongbo Chen,[1,2] Junkun Pan,[3,4] Disha M. Gandhi,[5] Chris Dockendorff,[5] Qiang Cui,[6] Baron Chanda,[1,3,4,*] and Katherine A. Henzler-Wildman[1,2,*]

[1]Graduate Program in Biophysics and [2]Department of Biochemistry, University of Wisconsin-Madison, Madison, Wisconsin; [3]Department of Neuroscience and [4]Department of Biomolecular Chemistry, School of Medicine and Public Health, University of Wisconsin-Madison, Madison, Wisconsin; [5]Departments of Chemistry, Marquette University, Milwaukee, Wisconsin; and [6]Departments of Chemistry, Physics, Biomedical Engineering, Boston University, Boston, Massachusetts

ABSTRACT The voltage-sensing domain (VSD) is a conserved structural module that regulates the gating of voltage-dependent ion channels in response to a change in membrane potential. Although the structures of many VSD-containing ion channels are now available, our understanding of the structural dynamics associated with gating transitions remains limited. To probe dynamics with site-specific resolution, we utilized NMR spectroscopy to characterize the VSD derived from *Shaker* potassium channel in 1-palmitoyl-2-hydroxy-sn-glycero-3-phospho-(1'-rac-glycerol) (LPPG) micelles. The backbone dihedral angles predicted based on secondary chemical shifts using torsion angle likeliness obtained from shift (TALOS+) showed that the *Shaker*-VSD shares many structural features with the homologous Kv1.2/2.1 chimera, including a transition from α-helix to 3_{10} helix in the C-terminal portion of the fourth transmembrane helix. Nevertheless, there are clear differences between the *Shaker*-VSD and Kv1.2/2.1 chimera in the S2-S3 linker and S3 transmembrane region, where the organization of secondary structure elements in *Shaker*-VSD appears to more closely resemble the KvAP-VSD. Comparison of microsecond-long molecular dynamics simulations of Kv 1.2-VSD in LPPG micelles and a 1-palmitoyl-2-oleoyl-glycero-3-phosphocholine (POPC) bilayer showed that LPPG micelles do not induce significant structural distortion in the isolated voltage sensor. To assess the integrity of the tertiary fold, we directly probed the binding of BrMT analog 2-[2-({[3-(2-amino-ethyl)-6-bromo-1H-indol-2-yl]methoxy}k7methyl)-6-bromo-1H-indol-3-yl]ethan-1-amine (BrET), a gating modifier toxin, and identified the location of the putative binding site. Our results suggest that the *Shaker*-VSD in LPPG micelles is in a native-like fold and is likely to provide valuable insights into the dynamics of voltage-gating and its regulation.

SIGNIFICANCE The *Shaker* potassium channel is a model for studying voltage-gating mechanisms within ion channels, but a high-resolution structure is lacking. We have developed a robust system for overexpression, purification, and structural characterization of the isolated *Shaker* voltage-sensing domain (VSD), which enables further biophysical and structural analysis and deeper understanding of this important system. Our initial NMR characterization of the *Shaker*-VSD reveals important and interesting structural features of the *Shaker*-VSD that do not match the structure predicted by homology models based on the Kv1.2/2.1 chimera crystal structure. Moreover, our NMR results reveal inherent structural flexibility within the isolated *Shaker*-VSD, which might help explain why the isolated *Shaker*-VSD is able to conduct proton currents in the absence of the pore domain.

INTRODUCTION

Voltage-sensing domains (VSDs) play a fundamental role in the gating processes of voltage-gated ion channels (1). They function to sense changes in membrane voltage, control the opening and closing of these channels, and generate electrical signals. So far, all known VSDs share a conserved architecture as well as a voltage-sensing mechanism (2). The VSD is composed of four consecutive transmembrane helixes (S1-S4) and is connected to the tetrameric pore domain via a short amphipathic linker helix. Conserved positively charged arginines are found on the S4 transmembrane helix (3,4), and their interaction with the membrane potential drives the movement of the

Submitted June 7, 2019, and accepted for publication June 20, 2019.

*Correspondence: chanda@wisc.edu or henzlerwildm@wisc.edu

Editor: Sudha Chakrapani.

Disha M. Gandhi's present address is University of North Carolina-Chapel Hill, Chapel Hill, North Carolina 27599.

https://doi.org/10.1016/j.bpj.2019.06.020

S4 transmembrane helix in response to voltage. As the VSDs are tightly coupled to the pore domain, the resulting conformational change in the VSDs regulates the state of the pore gate (5,6).

Numerous efforts using biochemical, electrophysiological, spectroscopic, and structural techniques have been made to characterize VSDs in an isolated form as well as in the context of full-length ion channels (5,7–13). One of the most important model systems for functional studies of VSDs and the development of our current understanding of voltage-sensing and voltage-gating mechanisms has been the *Shaker* potassium channel, a voltage-gated K^+-selective channel from *Drosophila* (14–20). Two competing models for voltage-sensor movement, the transporter model and the helical screw model, have been proposed based on structural, electrophysiological, and computational studies of the *Shaker* ion channel and its homologs (21–28). Crystal and cryogenic electron microscopy (cryo-EM) structures of homologous ion channels (29–31) have been solved, but the structure of the *Shaker* potassium channel is not available. These channels differ mostly in their loop regions, which have been shown to be important for function and pharmacological specificity (32–36). Despite their importance, these linkers are either truncated or not visible in the available structures of homologous channels (35,37).

In this study, we describe the use of solution NMR spectroscopy to characterize the voltage-sensing domain of the *Shaker* potassium channel in 1-palmitoyl-2-hydroxy-sn-glycero-3-phospho-(1'-rac-glycerol) (LPPG) micelles. NMR spectroscopy is a powerful method for studying protein structure and dynamics with residue-level resolution (38–41), but the full-length tetrameric potassium channel solubilized in a membrane mimetic environment is too large for solution-phase NMR studies. The discovery of voltage-sensitive phosphatases and voltage-gated proton channels, both of which lack the canonical pore domain, shows that the VSDs of ion channels can function as independent structural modules (12,13). We find that the backbone structure of *Shaker*-VSD in LPPG micelles is generally consistent with the high-resolution structure of the homologous voltage-gated K^+ (Kv) channels. Our NMR structural analysis also reveals some features that were unexpectedly different from homology models based on the Kv1.2/2.1 chimera crystal structure, such as a longer S3 helix in the *Shaker*-VSD. Binding of the gating modifier toxin BrMT analog 2-[2-({[3-(2-amino-ethyl)-6-bromo-1H-indol-2-yl]methoxy}k7methyl)-6-bromo-1H-indol-3-yl]ethan-1-amine (BrET) to the isolated VSDs suggests that the tertiary structural fold is properly maintained in LPPG micelles and also reveals details about the toxin binding site in these channels. Overall, the results provided here show that isolated *Shaker*-VSD may be a suitable system for further studies of structural dynamics of voltage-sensing domains.

MATERIALS AND METHODS

Cloning and overexpression of *Shaker*-VSD

Codon-optimized segments of *Shaker* (222–392, 208–380, 208–392, 208–397, or 217–397) with an N-terminal 8xHis tag followed by TEV protease cleavage site were cloned into a pET15b expression vector. To optimize the overexpression of the *Shaker*-VSD, pET15b-*Shaker*-VSD constructs were transformed into *Escherichia coli* BL21 (DE3) with pRARE plasmids for additional codon supply. Overexpression of *Shaker*-VSD was tested at three temperatures (16, 25, and 37°C) and three isopropyl β-D-1-thiogalactopyranoside concentrations (0.1, 0.5, and 1 mM) at OD 0.8–1.0 in M9 minimal media. The expression levels were evaluated using 14% sodium dodecyl sulphate-polyacrylamide gel electrophoresis (SDS-PAGE). Segment 217–397 overexpressed at 25°C and induced overnight (18–20 h) with 0.5 mM isopropyl β-D-1-thiogalactopyranoside gave the best yield and thus was used for protein production for NMR studies. For isotopic labeling with ^{13}C, ^{15}N, and/or ^{2}H, the standard media components were substituted with $^{15}NH_4Cl$, ^{13}C-glucose, and/or D_2O plus 0.5 g/L isotopically labeled isogro (Sigma-Aldrich, St. Louis, MO).

Reconstitution of *Shaker*-VSD into lysolipid micelles

To purify *Shaker*-VSD, cells were collected and resuspended in buffer A (50 mM Tris (pH 8.0), 100 mM KCl, 1 μg/mL pepstatin, 10 μM leupeptin, and 100 μM phenylmethylsulfonyl fluoride) with 1 mM EDTA, 5 mM β-me, 250 mM sucrose, and 1 mg/mL lysozyme and lysed by sonication. The cell debris and inclusion bodies were separated using a low speed spin (20 min at 7000 $\times$ g). The membrane fraction was isolated by spinning for 1 h at 150,000 $\times$ g. Detergent (40 mM n-decyl-β-D-maltopyranoside [DM], 40 mM n-dodecyl-β-D-maltopyranoside [DDM], 1% w/v n-octyl-β-D-glucopyranoside [OG], 1% w/v 3-[(3-cholamidopropyl)dimethylammonio]-1-propanesulfonate [CHAPS], or 1.5% w/v foscholine-12, Anatrace, Maumee, OH) and 15 mM tris(2-carboxyethyl)phosphine (TCEP) were added to buffer A to extract *Shaker*-VSD from the membrane fraction. After solubilizing for 2 h with rotation at room temperature, insoluble protein was removed by centrifugation at 30,000 $\times$ g for 30 min. Only DM and foscholine-12 were able to extract *Shaker*-VSD. As further fast protein liquid chromatography purifications indicate that *Shaker*-VSD aggregates in DM micelles but not foscholine-12 micelles (data not shown), foscholine-12 is chosen as the detergent for *Shaker*-VSD extraction. Solubilized *Shaker*-VSD in foscholine-12 was applied to Ni-NTA His-bind beads (Protino, Düren, Germany) prewashed with buffer B (50 mM Tris (pH 8.0), 100 mM KCl, and 15 mM TCEP), supplemented with 0.15% w/v foscholine-12, and allowed to bind for 30 min at room temperature. The beads were washed with 10 bed volumes of buffer B, followed by 10 bed volumes of buffer C (buffer B plus 20 mM imidazole and 0.15% w/v foscholine-12).

For reconstitution into lysolipid micelles, foscholine-12 was exchanged by washing the beads with 15 bed volumes of buffer B supplemented with 0.1% w/v 1-myristoyl-2-hydroxy-sn-glycero-3-phospho-(1'-rac-glycerol) (LMPG), LPPG, or 1-palmitoyl-2-hydroxy-sn-glycero-3-phosphocholine (LPPC). *Shaker*-VSD was eluted with five bed volumes of buffer B supplemented with 400 mM imidazole and 0.2% w/v LMPG, LPPG, or LPPC. For LPPG and LPPC reconstitution, eluted *Shaker*-VSD was dialyzed against TEV cleavage buffer (20 mM Tris (pH 8.0), 50 mM KCl, and 5 mM β-me) containing 0.0001% w/v LPPG or LPPC. For LMPG reconstitution, eluted *Shaker*-VSD was run through a PD-10 column equilibrated with TEV cleave buffer containing 0.2% w/v LMPG to remove imidazole. TEV protease was then added at 1:1 VSD/TEV mole ratio and incubated overnight at room temperature to remove His-tag. The next day, His-tag cleavage was verified using 14% SDS-PAGE. The solubilized and cleaved *Shaker*-VSD was then applied back to Ni-NTA His-bind resin to remove His-tagged TEV

protease and cleaved tag. The flow through was concentrated to 0.5 mL and loaded onto a Superdex 200 column pre-equilibrated in NMR buffer (100 mM MOPS (pH 7.0), 50 mM KCl, and 4 mM TCEP) with the appropriate detergent (0.2% w/v LMPG, LPPG, or LPPC). Peak fractions containing *Shaker*-VSD were pooled and concentrated to 300 μL for NMR. For *Shaker*-VSD in LPPG/LPPC mixed micelles, samples purified with LPPG and LPPC micelles were mixed at 1:1 volume ratio before concentration. For *Shaker*-VSD in LPPG/Chobimalt mixed micelles, Chobimalt was added before concentration.

Reconstitution of *Shaker*-VSD into bicelles

Expression of *Shaker*-VSD was the same except the TEV protease cleavage site was replaced with a thrombin cleavage site to achieve efficient His-tag cleavage in foscholine-12. The initial extraction and Ni-NTA resin binding steps are as described above. *Shaker*-VSD was eluted from the Ni-NTA resin as above and then concentrated to 0.5 mL aliquots for loading directly onto a Superdex 200 column pre-equilibrated in NMR buffer (100 mM MOPS (pH 7.0), 50 mM KCl, and 4 mM TCEP) with 10 mM foscholine-12. Peak fractions were pooled, and thrombin was added to remove the His-tag.

To reconstitute *Shaker*-VSD into bicelles, we used our previously published protocol with slight modifications (42). Long-chain lipids (Table S1) were hydrated at 20 mg/mL in NMR buffer, bath sonicated for ~1 min, and solubilized with 10 mM foscholine-12 for 20 min. Purified and cleaved *Shaker*-VSD fractions after size-exclusion purification were added to the solubilized long-chain lipids at a molar ratio of 1:100 VSD/lipids and rotated at room temperature for 3 h. Two aliquots of 45 mg Amberlite XAD-2 (Bio-Rad Laboratories, Hercules, CA) per milligram of total detergent were added to remove the detergent and incubated overnight at room temperature. Amberlite was removed by filtration, and the *Shaker*-VSD proteoliposomes were ultracentrifuged at 150,000 $\times$ *g* for 2 h at 6°C. The proteoliposome pellet was solubilized with short-chain lipids (Table S1) dissolved in NMR buffer to create q = 0.33 bicelles. Four freeze-thaw cycles produced homogeneous bicelles containing *Shaker*-VSD, which were flash frozen and stored at −80°C until use.

Reconstitution of *Shaker*-VSD into nanodiscs

MSP1D1ΔH5, a truncation mutant that produces nanodiscs with a smaller diameter, was used to assemble *Shaker*-VSD containing nanodiscs (43), with plasmids generously provided by Prof. Gerhard Wagner. The expression and purification of MSP1D1ΔH5 was performed according to the previously published protocol (44). The N-terminal His-tag was removed by TEV protease. Any additional His-tagged TEV protease was removed by applying back to Ni-NTA resin. His-tag cleavage and TEV removal were verified by SDS-PAGE.

Shaker-VSD was purified following the bicelle reconstitution protocol described above except that the His-tag was not cleaved. Nanodiscs were assembled according to established protocols with modifications (43–45). Briefly, MSP1D1ΔH5 and foscholine-12 solubilized lipids (Table S1) were incubated with *Shaker*-VSD at a molar ratio of VSD/MSP1D1ΔH5/lipid of 1:20:200 overnight at room temperature in 50 mM Tris (pH 8.0), 100 mM KCl, 4 mM TCEP, and 100 mM foscholine-12. The next day, three aliquots of 10 mg Amberlite XAD-2 (Bio-Rad Laboratories) per milligram of total detergent were added to remove the detergent, with incubation 4–12 h at room temperature after each addition. Amberlite was removed by filtration, and the nanodisc-containing solution was incubated with Ni-NTA beads at room temperature for 30 min to separate *Shaker*-VSD containing nanodiscs. The Ni-NTA beads were then washed with 10 bed volumes of buffer B followed by 10 bed volumes of buffer D (buffer B plus 20 mM imidazole). VSD-containing nanodiscs were eluted with five bed volumes of elution buffer (buffer B plus 400 mM imidazole). Elutions were concentrated to 0.5 mL and loaded onto a Superdex 200 column pre-equilibrated in NMR buffer (100 mM MOPS (pH 7.0), 50 mM KCl, and 4 mM TCEP). Peak fractions were pooled and concentrated to 300 μL for NMR sample.

Reconstitution of *Shaker*-VSD into Amphipol A8-35

Shaker-VSD was reconstituted into Amphipol A8-35 according to the published protocol (46). *Shaker*-VSD was purified the same way as for bicelle reconstitution and mixed with A8-35 polymer at a mass ratio VSD/A8-35 of 1:5 and incubated at room temperature for 1 h. Two aliquots of 10 mg Amberlite XAD-2 (Bio-Rad Laboratories) per milligram of total detergent were added to remove the detergent with an incubation for 2 h at room temperature after each addition. Amberlite was removed by filtration, and the *Shaker*-VSD in A8-35 was concentrated to 0.5 mL and loaded onto a Superdex 200 column pre-equilibrated in NMR buffer (100 mM MOPS (pH 7.0), 50 mM KCl, and 4 mM TCEP). Fractions containing *Shaker*-VSD were pooled and concentrated to 300 μL for an NMR sample.

NMR experiments for the screening of membrane mimetics and assignment of backbone resonance

NMR samples contained 0.2–0.5 mM *Shaker*-VSD in various membrane mimetics with 10% D_2O and 5% NaN_3. Spectra were acquired at the National Magnetic Resonance Facility at Madison (University of Wisconsin-Madison, Madison, WI). Transverse relaxation optimized spectroscopy (TROSY)-HNCO, TROSY-HN(ca)CO, TROSY-HNCA, TROSY-HN(co)CA, and TROSY-HNCACB were analyzed on a 750-MHz Bruker spectrometer with cryoprobe and processed using NMRPipe (47) and analyzed with CCPNMR Analysis (48). Backbone walk experiments were supplemented with 1-^{13}C′-amino acid-specific labeling (49). The backbone assignments have been deposited in the BioMagResBank (http://www.bmrb.wisc.edu) as BMRB: 27886.

NMR-detected BrET binding studies

BrET-observed one-dimensional ^{1}H spectra with titrated *Shaker*-VSD were recorded on a 600-MHz Bruker spectrometer. Samples contained 0.1 mM BrET and 0.2% w/v (~3.9 mM) LPPG in NMR buffer in a 1.7-mm NMR tube at 25°C to track *Shaker*-VSD concentration-dependent chemical shift perturbations of the H_N in the indole ring of BrET. Because the *Shaker*-VSD and BrET have extremely limited solubility in water and are only soluble within the detergent micelles, traditional concentration units using the total sample volume are not appropriate. Instead, the mole fraction of *Shaker*-VSD and BrET in each sample was calculated relative to the moles of LPPG in each sample. The NMR chemical shift perturbation data were fit to determine the binding affinity using the equation below (50):

$$\Delta\omega_{obs} = \Delta\omega_{max}\left\{\left([P]_t + [L]_t + K_d\right) - \left[\left([P]_t + [L]_t + K_d\right)^2 - 4[P]_t + [L]_t\right]^{1/2}\right\}\Big/2[L][L]_t, \quad (1)$$

where $\Delta\omega_{obs}$ is the observed chemical shift perturbation of H_N, $\Delta\omega_{max}$ is the maximal chemical shift perturbation, $[P]_t$ is the total concentration of *Shaker*-VSD in each sample in mole percentage relative to LPPG, $[L]_t$ is the BrET concentration in mole percentage relative to LPPG, and K_d is the molar percentage binding affinity.

TROSY-HNCO spectra of *Shaker*-VSD without BrET were recorded with ~0.2 mM *Shaker*-VSD under the same conditions on a 750-MHz Bruker spectrometer. After the recording of TROSY-HNCO spectrum without BrET, 0.5 mg lyophilized BrET was incubated with the NMR sample overnight at room temperature (final molar percentage concentration relative to LPPG is ~9%), and the TROSY-HNCO spectrum was re-recorded. Chemical shift perturbation and peak volume were analyzed using CCPNMR Analysis (48).

Molecular dynamics simulations

Crystal structure of Kv1.2-VSD (Protein Data Bank [PDB]: 3LUT) (51) served as the starting structure. The initial Kv1.2-VSD LPPG micelle model and Kv.2-VSD 1-palmitoyl-2-oleoyl-glycero-3-phosphocholine (POPC) bilayer model were built with the web-based program CHARMM-GUI (52–54). For the micelle model, 150 LPPG molecules were added around the Kv1.2-VSD to form a torus-shaped micelle. The protein-micelle complex was solvated in a cube box of water with a side length of 115 Å. For the bilayer model, Kv1.2-VSD was embedded in a POPC lipid bilayer with a side length of 80 Å. A water box with a thickness of 15 Å was added to the top and the bottom of the lipid bilayer, and 150 mM KCl ions were randomly placed in the water.

Both simulations used the OpenMM package (55) with GPU-acceleration. The CHARMM36 force field (56,57) with TIP3P water model (58) was applied in constant particle number, pressure, and temperature ensemble. The system was first energy minimized for 500 steps. Then, a six-step equilibration was carried out before the production simulation with decreasing constraint forces on the backbone carbons, side chain heavy atoms, and micelle/lipid bilayer as recommended by CHARMM-GUI (59,60). Production simulations were carried out for 1000 ns at 298 K. Langevin Integrator was used with 1-fs time step and a collision frequency of 1 ps^{-1}. MonteCarloBarostat was applied at 1 atm with a frequency of 100 fs^{-1}. Nonbonded method used in the simulation was particle-mesh Ewald (PME) with a nonbonded cutoff of 12 Å and a switch distance of 10 Å. Bonds to hydrogens were constrained, and rigidWater option was implemented. Finally, periodic boundary condition was implemented at the edge of the water box.

RESULTS

Isolated *Shaker* voltage-sensing domain is properly folded in LPPG micelles and is suitable for NMR study

To determine the conditions for studying isolated *Shaker*-VSD using NMR, we screened various truncation segments of the *Shaker* channel, testing five different constructs spanning the voltage-sensing domain for expression in *E. coli* (BL21) (Fig. S1). Only segment 217–397 gave a high-level expression (Fig. 1, *a* and *b*); the other tested constructs did not express sufficiently for detection on SDS-PAGE with coomassie blue stain, indicating yields well below the amounts needed for NMR. Thus, this construct, hereafter referred to as *Shaker*-VSD, was used for all further studies. We then screened 31 different membrane mimetics to determine the optimal conditions for NMR (Table S1), as assessed by the number of resolved signals, peak dispersion, resolution, and uniformity of peak intensity across the ^{1}H-^{15}N TROSY-heteronuclear single quantum coherence (HSQC) spectrum. The best ^{1}H-^{15}N TROSY-HSQC spectra were obtained in LPPG and LMPG detergent micelles at 45°C, which is consistent with NMR studies of isolated VSDs from other ion channels (Figs. S2 and S3; (45,61–65)). The ^{1}H-^{15}N TROSY-HSQC spectra obtained in other membrane mimetics had fewer peaks or worse resolution, indicating a lack of stable, well-folded tertiary structure, and thus were excluded from further NMR study (Fig. S3).

NMR chemical shifts are highly sensitive to local structure, which affects the distribution of electrons around a nucleus and thus the shielding of the nucleus from the applied magnetic field of the spectrometer. Backbone chemical shifts are particularly sensitive to backbone torsion angles, hydrogen bonding, and primary amino acid sequence (66,67). The backbone torsion angle and secondary structure propensity of a protein can thus be predicted based on the backbone chemical shift data and the known amino acid sequence. The torsion angle likeliness obtained from shift (TALOS)+ program uses the empirical relationship between backbone ^{13}C, ^{15}N, and ^{1}H chemical shifts and backbone φ and ψ angles to reliably predict the backbone dihedral angles and secondary structure elements in proteins. Comparison of backbone torsion angles predicted from the NMR chemical shift data with the corresponding crystal structure across a 200-protein data set revealed significant deviations for only 2.5% of residues, some of which likely reflect actual structural differences between the solution and the crystal (68). This demonstrates the accuracy of chemical shift-based torsion angle prediction, and this approach is widely used in NMR structure calculation (69,70). Therefore, to check that *Shaker*-VSD was properly folded in LPPG detergent micelles, we first performed backbone assignment for secondary structure evaluation. 86% of the backbone amide resonances were assigned for *Shaker*-VSD with TROSY-HNCO, HN(ca)CO, HNCA, HN(co)CA, and HNCACB NMR experiments plus 1-$^{13}C'$ Gly, Phe, Ala, Tyr, Leu, Ile, and Val specifically labeled samples (Figs. 1 and S4; (49)). The secondary structure of *Shaker*-VSD was calculated by TALOS+ using the chemical shifts of backbone HN, ^{15}N, ^{13}CO, $^{13}C\alpha$, and $^{13}C\beta$ (68), and the dihedral angles were found to be most consistent with the expected secondary structural features observed in the Kv 1.2/2.1 chimera and full-length KvAP (Figs. 2 *a* and S5; (7,29,30)). As noted previously, the S4 transmembrane helix switches from α-helix to a 3_{10}-helix toward the C-terminus. Given the high homology between the Kv 1.2/2.1 chimera and *Shaker* channel in this region, we might expect that the *Shaker*-VSD will also exhibit this feature. Remarkably, we find that the NMR-derived backbone dihedral angles predicted by TALOS+ are consistent with classic 3_{10}-helix throughout the C-terminal end of the S4 transmembrane helix (Fig. 2, *b* and *c*).

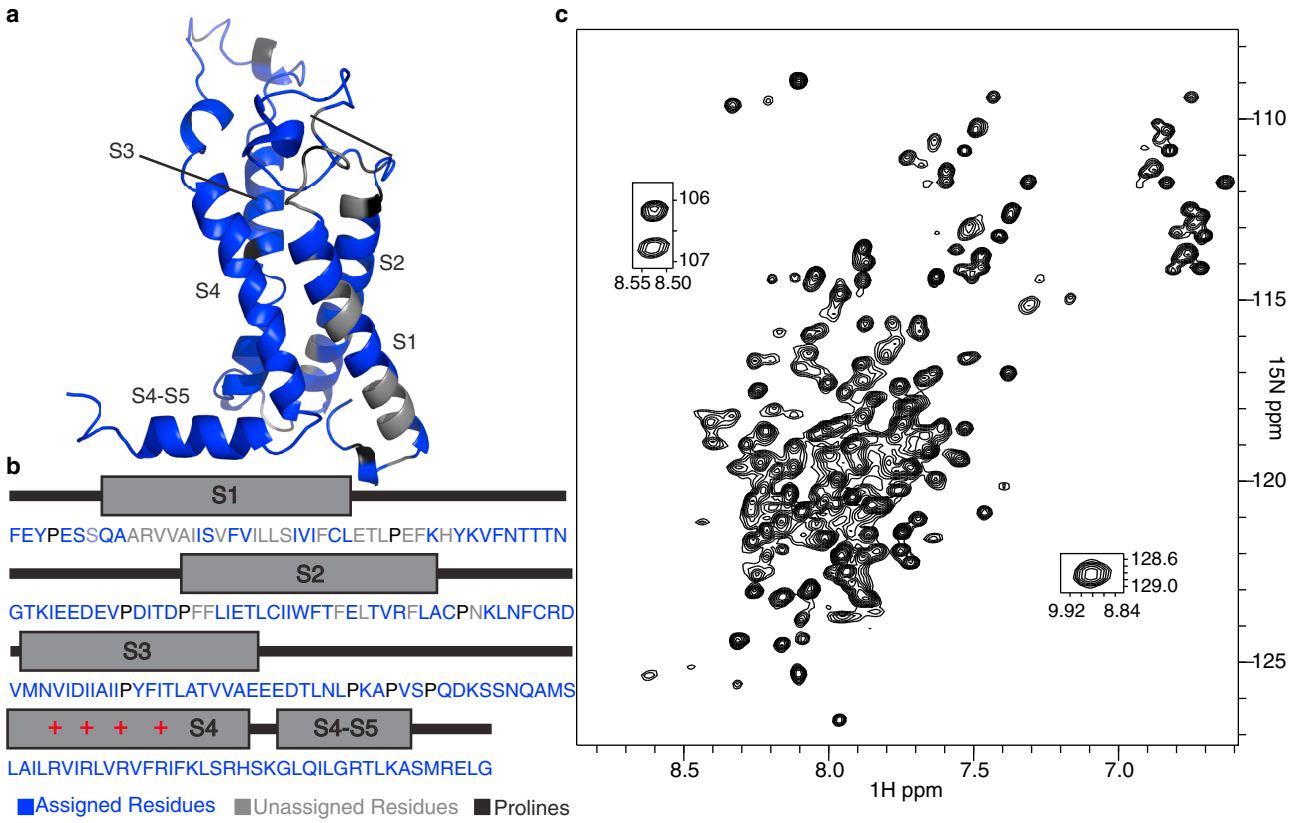

FIGURE 1 Isolated *Shaker*-VSD construct optimized for NMR study. (*a*) Shown is a homology model and (*b*) amino acid sequence of the isolated *Shaker*-VSD (217–397), which spans from the S1 transmembrane helix to the S4-S5 linker. Residues with assigned backbone resonances are colored blue. Prolines are colored black. Unassigned residues are colored gray. (*c*) ^{1}H-^{15}N TROSY-HSQC NMR spectrum of the isolated *Shaker*-VSD construct in LPPG micelle at pH 7.0 and 45°C is shown. Sequence assignments are shown in Fig. S4.

Next, we probed the integrity of the tertiary structure of isolated VSD by assaying its ability to bind the toxin BrET (Fig. 3 *a*). BrET is a synthetic derivative of a naturally occurring gating modifier gastropod toxin BrMT (6-bromo-2-mercaptotryptamine) (71). BrMT induces cooperativity in the *Shaker* potassium, presumably by interacting with the VSD (72). The BrMT binding site is proposed to lie within the S1, S2, and/or S3 transmembrane helices, but its binding has not been measured directly (71–74). We performed separate NMR experiments monitoring either BrET- or

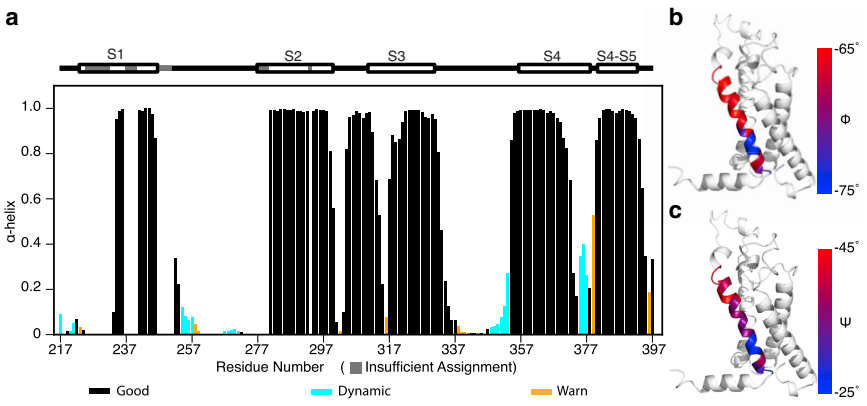

FIGURE 2 Secondary structure and backbone dihedral angles of the isolated *Shaker*-VSD. TALOS+ analysis of the backbone NMR chemical shifts (H_N, N, Co, Cα, and Cβ) can reliably predict the backbone dihedral angles and secondary structure elements in proteins. The α-helical propensity of the isolated *Shaker*-VSD under the conditions used for NMR studies is shown in (*a*), with numbering according to the full-length *Shaker* sequence. The expected secondary structure is shown above the data with lines and helices designating loops and rectangles, respectively, and regions with insufficient chemical shift assignments for TALOS+ analysis are drawn in gray. For the predicted α-helical propensity, bars are colored according to the quality of prediction indicated by TALOS+, with black indicating good prediction, cyan indicating dynamic conformations, and orange indicating ambiguous prediction. The data correspond quite well with the expected helical segments. The backbone dihedral angles, φ (*b*) and ψ (*c*), of the S4 transmembrane helix are plotted on the homology model of isolated *Shaker*-VSD with a blue to red color scale to illustrate that the reduced α-helical propensity in the C-terminal half of S4 is due to a transition to 3_{10}-helix. Backbone dihedral angles characteristic of α-helix are colored red, and torsion angles characteristic of 3_{10}-helix are colored blue in both (*b*) and (*c*).

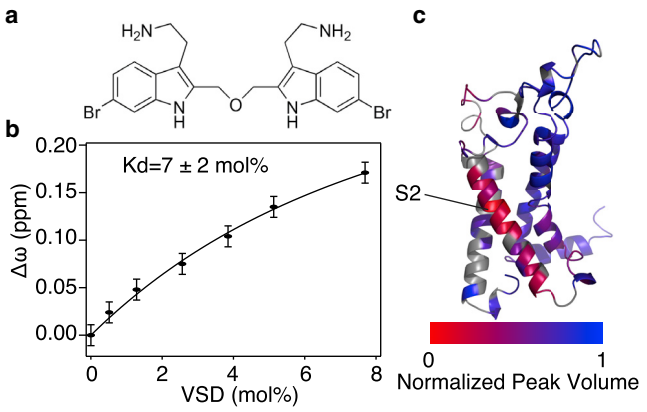

FIGURE 3 BrET interacts directly with *Shaker*-VSD. (*a*) Chemical structure of BrET is shown. (*b*) Binding curve was generated from NMR titration of BrET with the *Shaker*-VSD. The BrET ^{1}H NMR spectra used to generate this curve are shown in Fig. S8. (*c*) The addition of BrET to the isolated *Shaker*-VSD causes a localized perturbation of the three-dimensional TROSY-HNCO NMR spectrum, indicating a specific binding interaction. The normalized change in peak volume in the *Shaker*-VSD upon BrET binding is plotted on a homology model of the isolated *Shaker*-VSD with a blue to red color scale as shown. Significant peak volume reduction is observed for residues from S2 transmembrane helix. Small chemical shift perturbations are also observed, as shown in Fig. S7.

Shaker-VSD to confirm direct and specific binding of BrET to *Shaker*-VSD at 25°C. Specific chemical shift perturbation of a well-resolved BrET peak corresponding to the −NH group in the indole ring was observed upon titration with unlabeled *Shaker*-VSD. Fitting this data yields an apparent binding affinity of 7 ± 2 mol% (Figs. 3 *b* and S6). Results are reported as mol% because the highly hydrophobic BrET has minimal solubility in water and is only soluble in the LPPG micelles. Given that most of the VSD is likely to be in an activated conformation in the absence of membrane potential, it is not surprising that the BrET, which has a preference for the resting conformation (72,74), binds weakly to the isolated VSD.

To further identify the binding site of BrET within *Shaker*-VSD, we recorded three-dimensional TROSY-HNCO spectra of *Shaker*-VSD with and without BrET at 45°C. We observed a significant volume reduction of peaks from residues on the S2 transmembrane helix (Fig. 3 *c*). BrET was previously hypothesized to bind to the same region based on electrophysiology studies (71,72,74). The significant line broadening and loss of peak intensity observed upon BrET addition is consistent with the rapid on and off of a weak binding ligand coupled with a structural transition upon ligand binding (75). Moreover, we also observed a small but significant chemical shift perturbation throughout the entire protein (Fig. S7), suggesting that the protein undergoes a global conformational change upon binding. These results confirm direct binding of BrET to *Shaker*-VSD with the binding site centered on the S2 helix, indicating that the architecture of the toxin binding site in isolated *Shaker*-VSD in LPPG micelles is conserved.

Multiple structural states of the isolated *Shaker*-VSD

Upon assigning the backbone resonances of *Shaker*-VSD, we observed peak doubling for residues in the S0 helix, S1-S2 linker, S4 transmembrane helix, and S4-S5 linker in the TROSY-HNCO and HNCA spectra (Fig. S8). This indicates that these regions of *Shaker*-VSD exist in two distinct conformations under our NMR experimental condition. One possibility is that these reflect the resting and activated states of the isolated VSDs, but charge-voltage measurements of *Shaker*-VSD shows that these channels are more than 90% activated at 0 mV (76). Alternatively, the isolated voltage sensors are known to undergo a transition into a relaxed state upon prolonged activation (77). Because these isolated domains do not experience any voltage gradient in the micelles, it is quite likely that the observed peak doubling particularly in the S4 and S4-S5 linker reflects the conformational transitions between the activated and relaxed states. Nevertheless, additional experiments would be necessary to determine whether these conformational transitions correspond to the functional states identified by electrophysiologists. In any case, the observation of peak doubling highlights the inherent flexibility of this region of the VSD and exactly where the functionally relevant structural transitions are expected to occur.

Inherent structural features of *Shaker*-VSD

The crystal structure of Kv1.2/2.1 chimera has been widely used as a model for functional studies of *Shaker* potassium channel (6,20,78–80). Because of their highly conserved sequences, the structure of *Shaker*-VSD is expected to be almost identical to that of Kv1.2/2.1 chimera, except for S1-S2 and S3-S4 linker whose length and sequence are very different. As previously noted, the NMR-derived backbone torsion angles are consistent with a transition from α-helix to 3_{10}-helix in the C-terminal portion of S4 as observed in Kv1.2/2.1. The NMR chemical shift-based secondary structure prediction also shows that the *Shaker* S3 transmembrane helix is composed of two individual helices (Fig. S3, *a* and *b*) like Kv 1.2/2.1(Figs. 2 *a* and S5). However, S3b is ∼1–2 helical turns longer and is separated from S3a by a short S3 loop in *Shaker*, and the loop between S2 and S3 helices is about seven residues shorter in *Shaker*-VSD than in Kv1.2/2.1-VSD. At this point, it is not clear whether these observed structural differences between the *Shaker* and Kv1.2/2.1 chimera are due to differences in detergents, primary structure, or both.

To test whether the LPPG detergent micelles can alter the VSD conformation, we performed molecular dynamics (MD) simulations of the VSD of Kv1.2 in both LPPG micelles and POPC bilayer for comparison. These simulations were performed with the Kv1.2 because of the availability of the high-resolution structural model (51). We extracted

the average backbone dihedral angles and their variances from 1 μs MD trajectories for comparison with the NMR data. We focused our comparison on the transmembrane helices because the sequences of the transmembrane helices are highly conserved between *Shaker*-VSD and Kv1.2-VSD. The length and sequence in the loop regions of *Shaker*-VSD vary significantly from that of Kv1.2-VSD (Figs. 4 and S9), so we excluded these regions from the analysis. Except for a few residues at the beginning and end of each transmembrane helix, no major secondary structure differences were observed between Kv1.2-VSD in LPPG micelles and POPC bilayer. Therefore, these observations support the notion that the LPPG micelles are unlikely to distort the secondary structure differences of the isolated voltage sensors.

We further compared the secondary structure of isolated *Shaker*-VSD with high-resolution x-ray and cryo-EM structures or NMR studies of other Kv-VSDs (7,29,30,63,81–83). Despite an overall conserved four-helix bundle architecture, we observed significant secondary structural diversity especially in the S3 transmembrane helix (Figs. 5 and S10). KCNQ1 has a straight S3 helix ~5 helical turns long, both in humans and *Xenopus* (63,83). In the cryo-EM structure of *X. laevis* KCNQ1-VSD, the linker connecting the S2 and S3 segments, is observed to form a short helix that is denoted as the S2/S3 helix. However, this is not present in isolated hKCNQ1-VSD, according to torsion angles derived from NMR secondary chemical shift analysis using TALOS+. rEAG-VSD and hHCN1-VSD share similar secondary structural configurations in this region (81,82). The S3b helices are ~3–4 helical turns long, with an unstructured region connecting the S3a and the S3b helices following a proline residue. A Thr or Ser in the middle of the S3a helix breaks it into two subhelices, each of which are ~3 helical turns long and is denoted as S3a1 and S3a2, respectively. The crystal and cryo-EM structures of the Kv1.2/2.1 chimera-VSD obtained in different membrane mimetics (detergent/lipid mixed micelles and nanodiscs, respectively) are almost identical to each other but show differences compared to the rEAG and hHCN channel structures (29,30). The S3 helix in Kv1.2/2.1 chimera is also broken into S3a and S3b following a proline residue, but the S3a is not further subdivided into smaller helices. This architecture is similar to the KvAP-VSD in which the bend between the S3a and S3b helix is more pronounced. Overall, the backbone torsion angles and secondary structure assignments based on NMR secondary chemical shift analysis are in agreement with the high-resolution structures of related channels, which strongly indicate that the isolated *Shaker*-VSD in LPPG micelles is in a native-like fold. The backbone structure of the *Shaker*-VSD is similar to the Kv1.2/2.1 chimera as expected, particularly in the charged residue containing S4 helix. In contrast, comparison of the variable S3 helix (Figs. 5, S5, and S11) suggests that the length of S3a and S3b and the size of the

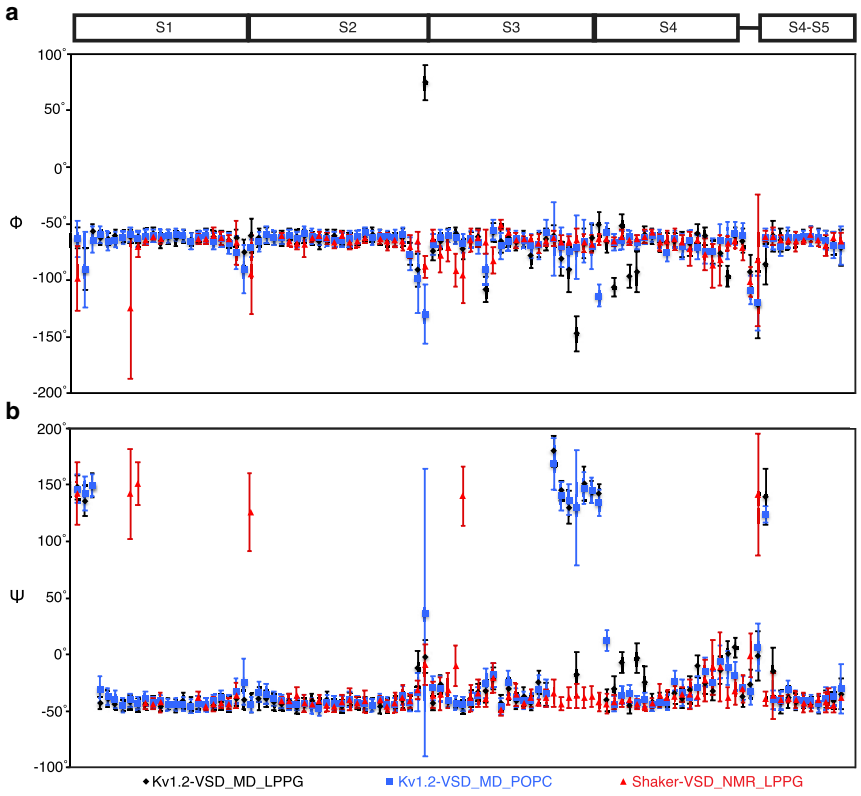

FIGURE 4 Comparison *Shaker*-VSD with simulated backbone torsion angles of Kv1.2-VSD. MD simulations of Kv1.2-VSD were performed in both LPPG micelle and POPC bilayers to evaluate the effect of the micelle environment on the VSD structure. Kv1.2-VSD was chosen because of its homology to *Shaker* and the availability of a crystal structure. Backbone (*a*) φ and (*b*) ψ torsion angles are shown for helical segments in which the homology between *Shaker*-VSD and Kv1.2-VSD is high (sequence alignment shown in Fig. S9). Comparison of backbone torsion angles of Kv1.2-VSD after 1 μs MD simulations in LPPG micelles (*black*) and POPC bilayers (*blue*) shows that they are nearly identical, indicating that the lysolipid micelle does not significantly distort the VSD structure. The experimentally determined backbone torsion angles for *Shaker*-VSD in LPPG micelles (*red*, data from Fig. 2) also match the Kv1.2-VSD simulation data, except where there are sequence differences between *Shaker* and Kv1.2.

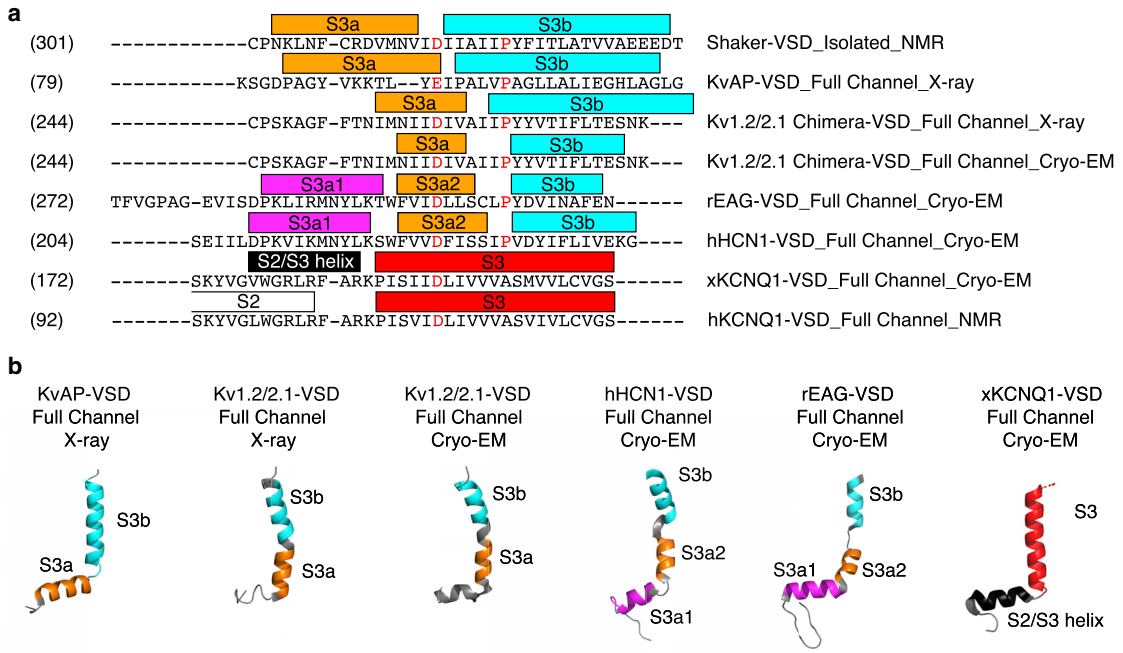

FIGURE 5 Diversified secondary structure configuration of S2-S3 linker and S3 helix in different Kv-VSDs. (*a*) Sequence alignment of the S2-S3 linker and S3 helix region of different Kv-VSDs is shown. Colored rectangles above the sequences indicate the segments corresponding to S3a1 (*magenta*), S3a2 (*orange*), S3b (*cyan*), straight S3 helix (*blue*), S2-S3 helix (*gray*), or S2 helix (*white*). Backbone φ and ψ angles extracted from the Protein Data Bank structures were extracted and analyzed (Ramachandran plots in Fig. S10) to define the helical regions: isolated *Shaker*-VSD (our NMR results); KvAP-VSD in full channel, x-ray (1ORQ); Kv1.2/2.1-VSD in full channel, x-ray (2R9R); Kv1.2/2.1-VSD in full channel, cryo-EM (6EBK); human KCNQ1-VSD, NMR; *X. laevis* KCNQ1-VSD in full channel, cryo-EM (5VMS); EAG-VSD in full channel, cryo-EM (5K7L); and HCN1-VSD in full channel, cryo-EM (5U6O). (*b*) The defined helical regions are shown in the same color scheme plotted on the segment of the structure corresponding to the sequence alignment in (*a*) for each of the different Kv-VSDs, highlighting the structural diversity in this region. Comparison of the variable S3 helix (also Figs. S5 and S11) suggests that the length and position of helices within this region in *Shaker*-VSD might be more similar to KvAP.

intervening loop in *Shaker*-VSD might be more similar to KvAP. However, the current data are insufficient to evaluate whether the angle between the S3a and S3b helices matches full-length KvAP.

DISCUSSION

The *Shaker* potassium channel is a model system for studying the mechanisms of voltage gating and regulation. It is well characterized mainly in terms of its electrophysiological behavior, but very little is known about the structure of these channels. The related Kv 1.2/2.1 chimera high-resolution structure is widely used as a model for interpreting the functional effects of structural perturbations. Nevertheless, it is clear that there are significant differences between the *Shaker* and Kv 1.2 channels. For instance, Islas et al. have shown that the Kv 1.2 channels move ~25% less charge than the *Shaker* potassium channel in response to a depolarizing voltage pulse (84). Biophysical and structural characterization of *Shaker*-VSD has been hindered, in part, by the difficulty in obtaining milligram quantities of properly folded and functional samples (85). In this study, we have generated a robust protocol for heterogeneous overexpression and purification of isolated *Shaker*-VSD. We assessed the structural integrity of the *Shaker*-VSD in 31 different membrane mimetics (86–88) and found conditions suitable for NMR studies. Among all the membrane mimetics that were screened, the best ^{1}H-^{15}N TROSY-HSQC spectra were obtained in lysophosphatidylglycerol (LMPG and LPPG) detergent micelles. The secondary structure predicted from our backbone resonance assignments, as well as the BrET binding studies, support a native-like fold for *Shaker*-VSD in LPPG micelles. Interestingly, LPPG micelles have also been used for NMR studies of the VSDs of KCNQ1, Na_v 1.4, and hERG as well as the sensing domain of TRPM8 (45,61–64), suggesting that Lyso-PG detergent micelles are best suited for studying isolated VSDs.

Although the overall secondary structure of the *Shaker* potassium channel is consistent with the structures of other closely related potassium channels such as Kv 1.2/2.1 chimera, there were a few notable differences. First, the increased length of the *Shaker* S3a and the S3b helices and their separation by a short unstructured loop region as well as the break within the S3a helix make this region more closely resemble the structure of KvAP than Kv1.2/2.1. Second, our studies reveal an inherent flexibility of the isolated *Shaker*-VSD. The ^{1}H-^{15}N TROSY-HSQC spectrum of isolated *Shaker*-VSD is crowded with

significant variation in peak intensity across the spectrum (Fig. 1 *c*). In contrast, the NMR peaks from isolated KvAP-VSD and hKCNQ1-VSD are well dispersed and more uniform (45,63,65,89). A single set of well-resolved resonances is the hallmark of a tightly packed, stable tertiary structure in which each residue is locked in a single unique environment. Protein motion leads to increased line broadening due to enhanced relaxation or the averaging effect of sampling multiple different structural states, depending on the timescale. Conformational heterogeneity and dynamic sampling of multiple states on microsecond-millisecond timescales also average the chemical shift for a single resonance across different environments and reduce chemical dispersion. For several regions of the *Shaker*-VSD, we also observed peak doubling, indicating that those regions in the channel are sampling at least two different conformations on a millisecond or slower timescale. This peak doubling further contributes to the crowding in the NMR spectra of *Shaker*-VSD and emphasizes the inherent dynamics of the *Shaker*-VSD. Recent electrophysiological studies of the isolated *Shaker*-VSD show that the voltage-sensing domain is able to conduct proton currents in the absence of pore domain, whereas these proton currents are not observed in the full-length channel (76). One interpretation is that in the absence of the stabilizing influence of the pore domain, the voltage-sensing domain of the *Shaker* potassium channel is more dynamic and allows protons to pass through. Note that inside the gating pore of the *Shaker*-VSD, the extracellular and the intracellular solutions are separated by a single aromatic charge transfer center. Therefore, it is not difficult to envision that this separation is not as tight in the isolated VSD. However, specific conclusions about whether the observation of proton current through isolated *Shaker*-VSD is related to the flexibility here by NMR is not possible without additional experiments. Comparison with equivalent data for KCNQ and KvAP-VSDs may be helpful in testing this hypothesis.

In conclusion, our study for the first time to our knowledge establishes a robust system for biochemical, biophysical, and structural study of isolated *Shaker*-VSD. We have characterized secondary structural features of the isolated *Shaker*-VSD using NMR spectroscopy and provided insight into the channel dynamics. Our studies also shed light on the binding site of a small-molecule gating modifier of the *Shaker* potassium channel, BrET. Follow-up studies will allow us to gain a deeper structural understanding of the *Shaker*-VSD for comparison with functional studies to gain more insight into the voltage-sensing mechanism of voltage-gated ion channels.

SUPPORTING MATERIAL

Supporting Material can be found online at https://doi.org/10.1016/j.bpj.2019.06.020.

AUTHOR CONTRIBUTIONS

H.C., B.C., and K.A.H.-W. designed the research. H.C. executed the experiments. H.C. and K.A.H.-W. analyzed the data. J.P. performed MD simulations and analyzed the data under the supervision of Q.C. and B.C. D.M.G. and C.D. synthesized BrET for BrET binding experiments. H.C., B.C., and K.A.H.-W. wrote the manuscript.

ACKNOWLEDGMENTS

We thank Scott Wildman for generating the homology model of *Shaker*-VSD, Marco Tonelli and Claudia Cornilescu for technical assistance with NMR experiments, Prof. Jon Sack for helpful communications and suggestions regarding BrET-related experiments, Prof. Gerhard Wagner for kindly proving the plasmids for MSP1D1 expression, Vilius Kurauskas for help generating Ramachandran plots, and Vadim Klenchin for help with protein expression and purification at the initial stage.

We thank the National Institutes of Health (NIH) for grant support NS081293 (B.C.). This study made use of the National Magnetic Resonance Facility at Madison, which is supported by NIH grant P41GM103399 (National Institute of General Medical Sciences) (old number: P41RR002301). Equipment was purchased with funds from the University of Wisconsin-Madison, the NIH P41GM103399, S10RR02781, S10RR08438, S10RR023438, S10RR025062, S10RR029220), the National Science Foundation (DMB-8415048, OIA-9977486, BIR-9214394), and the U.S. Department of Agriculture.

REFERENCES

1. Swartz, K. J. 2008. Sensing voltage across lipid membranes. *Nature.* 456:891–897.
2. Chanda, B., and F. Bezanilla. 2008. A common pathway for charge transport through voltage-sensing domains. *Neuron.* 57:345–351.
3. Lee, S. Y., A. Lee, …, R. MacKinnon. 2005. Structure of the KvAP voltage-dependent K+ channel and its dependence on the lipid membrane. *Proc. Natl. Acad. Sci. USA.* 102:15441–15446.
4. Payandeh, J., T. Scheuer, …, W. A. Catterall. 2011. The crystal structure of a voltage-gated sodium channel. *Nature.* 475:353–358.
5. Roux, B. 2006. Dissecting the coupling between the voltage sensor and pore domains. *Neuron.* 52:568–569.
6. Fernández-Mariño, A. I., T. J. Harpole, …, B. Chanda. 2018. Gating interaction maps reveal a noncanonical electromechanical coupling mode in the Shaker K^+ channel. *Nat. Struct. Mol. Biol.* 25:320–326.
7. Jiang, Y., A. Lee, …, R. MacKinnon. 2003. X-ray structure of a voltage-dependent K+ channel. *Nature.* 423:33–41.
8. Ruta, V., and R. MacKinnon. 2004. Localization of the voltage-sensor toxin receptor on KvAP. *Biochemistry.* 43:10071–10079.
9. Chakrapani, S., L. G. Cuello, …, E. Perozo. 2008. Structural dynamics of an isolated voltage-sensor domain in a lipid bilayer. *Structure.* 16:398–409.
10. Li, Q., S. Wanderling, …, E. Perozo. 2014. Structural basis of lipid-driven conformational transitions in the KvAP voltage-sensing domain. *Nat. Struct. Mol. Biol.* 21:160–166.
11. Cowgill, J., V. A. Klenchin, …, B. Chanda. 2019. Bipolar switching by HCN voltage sensor underlies hyperpolarization activation. *Proc. Natl. Acad. Sci. USA.* 116:670–678.
12. Ramsey, I. S., M. M. Moran, …, D. E. Clapham. 2006. A voltage-gated proton-selective channel lacking the pore domain. *Nature.* 440:1213–1216.
13. Li, Q., S. Wanderling, …, E. Perozo. 2014. Structural mechanism of voltage-dependent gating in an isolated voltage-sensing domain. *Nat. Struct. Mol. Biol.* 21:244–252.

14. Liman, E. R., P. Hess, …, G. Koren. 1991. Voltage-sensing residues in the S4 region of a mammalian K+ channel. *Nature.* 353:752–756.
15. Aggarwal, S. K., and R. MacKinnon. 1996. Contribution of the S4 segment to gating charge in the Shaker K+ channel. *Neuron.* 16:1169–1177.
16. Papazian, D. M., T. L. Schwarz, …, L. Y. Jan. 1987. Cloning of genomic and complementary DNA from Shaker, a putative potassium channel gene from Drosophila. *Science.* 237:749–753.
17. Hoshi, T., W. N. Zagotta, and R. W. Aldrich. 1994. Shaker potassium channel gating. I: transitions near the open state. *J. Gen. Physiol.* 103:249–278.
18. Zagotta, W. N., T. Hoshi, …, R. W. Aldrich. 1994. Shaker potassium channel gating. II: transitions in the activation pathway. *J. Gen. Physiol.* 103:279–319.
19. Zagotta, W. N., T. Hoshi, and R. W. Aldrich. 1994. Shaker potassium channel gating. III: evaluation of kinetic models for activation. *J. Gen. Physiol.* 103:321–362.
20. Tao, X., A. Lee, …, R. MacKinnon. 2010. A gating charge transfer center in voltage sensors. *Science.* 328:67–73.
21. Jiang, Y., V. Ruta, …, R. MacKinnon. 2003. The principle of gating charge movement in a voltage-dependent K+ channel. *Nature.* 423:42–48.
22. Long, S. B., E. B. Campbell, and R. Mackinnon. 2005. Voltage sensor of Kv1.2: structural basis of electromechanical coupling. *Science.* 309:903–908.
23. Jensen, M. O., D. W. Borhani, …, D. E. Shaw. 2010. Principles of conduction and hydrophobic gating in K+ channels. *Proc. Natl. Acad. Sci. USA.* 107:5833–5838.
24. Broomand, A., and F. Elinder. 2008. Large-scale movement within the voltage-sensor paddle of a potassium channel-support for a helical-screw motion. *Neuron.* 59:770–777.
25. Starace, D. M., E. Stefani, and F. Bezanilla. 1997. Voltage-dependent proton transport by the voltage sensor of the Shaker K+ channel. *Neuron.* 19:1319–1327.
26. Bezanilla, F. 2002. Voltage sensor movements. *J. Gen. Physiol.* 120:465–473.
27. Starace, D. M., and F. Bezanilla. 2004. A proton pore in a potassium channel voltage sensor reveals a focused electric field. *Nature.* 427:548–553.
28. Treptow, W., and M. Tarek. 2006. Environment of the gating charges in the Kv1.2 Shaker potassium channel. *Biophys. J.* 90:L64–L66.
29. Matthies, D., C. Bae, …, K. J. Swartz. 2018. Single-particle cryo-EM structure of a voltage-activated potassium channel in lipid nanodiscs. *eLife.* 7:e37558.
30. Long, S. B., X. Tao, …, R. MacKinnon. 2007. Atomic structure of a voltage-dependent K+ channel in a lipid membrane-like environment. *Nature.* 450:376–382.
31. Long, S. B., E. B. Campbell, and R. Mackinnon. 2005. Crystal structure of a mammalian voltage-dependent Shaker family K+ channel. *Science.* 309:897–903.
32. Mathur, R., J. Zheng, …, F. J. Sigworth. 1997. Role of the S3-S4 linker in Shaker potassium channel activation. *J. Gen. Physiol.* 109:191–199.
33. Gonzalez, C., E. Rosenman, …, R. Latorre. 2000. Modulation of the Shaker K(+) channel gating kinetics by the S3-S4 linker. *J. Gen. Physiol.* 115:193–208.
34. Gonzalez, C., E. Rosenman, …, R. Latorre. 2001. Periodic perturbations in Shaker K+ channel gating kinetics by deletions in the S3-S4 linker. *Proc. Natl. Acad. Sci. USA.* 98:9617–9623.
35. Priest, M. F., J. J. Lacroix, …, F. Bezanilla. 2013. S3-S4 linker length modulates the relaxed state of a voltage-gated potassium channel. *Biophys. J.* 105:2312–2322.
36. Sand, R., N. Sharmin, …, W. J. Gallin. 2013. Fine-tuning of voltage sensitivity of the Kv1.2 potassium channel by interhelix loop dynamics. *J. Biol. Chem.* 288:9686–9695.
37. Sørensen, J. B., A. Cha, …, F. Bezanilla. 2000. Deletion of the S3-S4 linker in the Shaker potassium channel reveals two quenching groups near the outside of S4. *J. Gen. Physiol.* 115:209–222.
38. Imai, S., M. Osawa, …, I. Shimada. 2010. Structural basis underlying the dual gate properties of KcsA. *Proc. Natl. Acad. Sci. USA.* 107:6216–6221.
39. Brettmann, J. B., D. Urusova, …, K. A. Henzler-Wildman. 2015. Role of protein dynamics in ion selectivity and allosteric coupling in the NaK channel. *Proc. Natl. Acad. Sci. USA.* 112:15366–15371.
40. Huang, H., G. Kuenze, …, C. R. Sanders. 2018. Mechanisms of KCNQ1 channel dysfunction in long QT syndrome involving voltage sensor domain mutations. *Sci. Adv.* 4:eaar2631.
41. Maruyama, T., S. Imai, …, M. Osawa. 2018. Functional roles of Mg^{2+} binding sites in ion-dependent gating of a Mg^{2+} channel, MgtE, revealed by solution NMR. *eLife.* 7:e31596.
42. Morrison, E. A., and K. A. Henzler-Wildman. 2012. Reconstitution of integral membrane proteins into isotropic bicelles with improved sample stability and expanded lipid composition profile. *Biochim. Biophys. Acta.* 1818:814–820.
43. Hagn, F., M. Etzkorn, …, G. Wagner. 2013. Optimized phospholipid bilayer nanodiscs facilitate high-resolution structure determination of membrane proteins. *J. Am. Chem. Soc.* 135:1919–1925.
44. Ritchie, T. K., Y. V. Grinkova, …, S. G. Sligar. 2009. Chapter 11 - reconstitution of membrane proteins in phospholipid bilayer nanodiscs. *Methods Enzymol.* 464:211–231.
45. Shenkarev, Z. O., E. N. Lyukmanova, …, A. S. Arseniev. 2010. Lipid-protein nanodiscs as reference medium in detergent screening for high-resolution NMR studies of integral membrane proteins. *J. Am. Chem. Soc.* 132:5628–5629.
46. Zoonens, M., F. Zito, …, J.-L. Popot. 2014. Amphipols: a general introduction and some protocols. Membrane Proteins Production for Structural Analysis. Springer, pp. 173–204.
47. Delaglio, F., S. Grzesiek, …, A. Bax. 1995. NMRPipe: a multidimensional spectral processing system based on UNIX pipes. *J. Biomol. NMR.* 6:277–293.
48. Vranken, W. F., W. Boucher, …, E. D. Laue. 2005. The CCPN data model for NMR spectroscopy: development of a software pipeline. *Proteins.* 59:687–696.
49. Takeuchi, K., E. Ng, …, G. Wagner. 2007. 1-13C amino acid selective labeling in a 2H15N background for NMR studies of large proteins. *J. Biomol. NMR.* 38:89–98.
50. Williamson, M. P. 2013. Using chemical shift perturbation to characterise ligand binding. *Prog. Nucl. Magn. Reson. Spectrosc.* 73:1–16.
51. Chen, X., Q. Wang, …, J. Ma. 2010. Structure of the full-length Shaker potassium channel Kv1.2 by normal-mode-based X-ray crystallographic refinement. *Proc. Natl. Acad. Sci. USA.* 107:11352–11357.
52. Jo, S., T. Kim, …, W. Im. 2008. CHARMM-GUI: a web-based graphical user interface for CHARMM. *J. Comput. Chem.* 29:1859–1865.
53. Cheng, X., S. Jo, …, W. Im. 2013. CHARMM-GUI micelle builder for pure/mixed micelle and protein/micelle complex systems. *J. Chem. Inf. Model.* 53:2171–2180.
54. Wu, E. L., X. Cheng, …, W. Im. 2014. CHARMM-GUI Membrane Builder toward realistic biological membrane simulations. *J. Comput. Chem.* 35:1997–2004.
55. Eastman, P., M. S. Friedrichs, …, V. S. Pande. 2013. Openmm 4: a reusable, extensible, hardware independent library for high performance molecular simulation. *J. Chem. Theory Comput.* 9:461–469.
56. MacKerell, A. D., D. Bashford, …, M. Karplus. 1998. All-atom empirical potential for molecular modeling and dynamics studies of proteins. *J. Phys. Chem. B.* 102:3586–3616.
57. Best, R. B., X. Zhu, …, A. D. Mackerell, Jr. 2012. Optimization of the additive CHARMM all-atom protein force field targeting improved sampling of the backbone φ, ψ and side-chain $\chi(1)$ and $\chi(2)$ dihedral angles. *J. Chem. Theory Comput.* 8:3257–3273.

58. Jorgensen, W. L., J. Chandrasekhar, …, M. L. Klein. 1983. Comparison of simple potential functions for simulating liquid water. *J. Chem. Phys.* 79:926–935.

59. Brooks, B. R., C. L. Brooks, III, …, M. Karplus. 2009. CHARMM: the biomolecular simulation program. *J. Comput. Chem.* 30:1545–1614.

60. Lee, J., X. Cheng, …, W. Im. 2016. Charmm-gui input generator for namd, gromacs, amber, openmm, and charmm/openmm simulations using the charmm36 additive force field. *J. Chem. Theory Comput.* 12:405–413.

61. Ng, H. Q., Y. M. Kim, …, C. Kang. 2012. Purification and structural characterization of the voltage-sensor domain of the hERG potassium channel. *Protein Expr. Purif.* 86:98–104.

62. Rath, P., J. K. Hilton, …, W. D. Van Horn. 2016. Implications of human transient receptor potential melastatin 8 (trpm8) channel gating from menthol binding studies of the sensing domain. *Biochemistry.* 55:114–124.

63. Peng, D., J. H. Kim, …, C. R. Sanders. 2014. Purification and structural study of the voltage-sensor domain of the human KCNQ1 potassium ion channel. *Biochemistry.* 53:2032–2042.

64. Paramonov, A. S., E. N. Lyukmanova, …, Z. O. Shenkarev. 2017. NMR investigation of the isolated second voltage-sensing domain of human Nav1.4 channel. *Biochim. Biophys. Acta Biomembr.* 1859:493–506.

65. Shenkarev, Z. O., A. S. Paramonov, …, A. S. Arseniev. 2010. NMR structural and dynamical investigation of the isolated voltage-sensing domain of the potassium channel KvAP: implications for voltage gating. *J. Am. Chem. Soc.* 132:5630–5637.

66. de Dios, A. C., J. G. Pearson, and E. Oldfield. 1993. Secondary and tertiary structural effects on protein NMR chemical shifts: an ab initio approach. *Science.* 260:1491–1496.

67. Spera, S., and A. Bax. 1991. Empirical correlation between protein backbone conformation and c.Alpha. And c.Beta. 13c nuclear magnetic resonance chemical shifts. *J. Am. Chem. Soc.* 113:5490–5492.

68. Shen, Y., F. Delaglio, …, A. Bax. 2009. TALOS+: a hybrid method for predicting protein backbone torsion angles from NMR chemical shifts. *J. Biomol. NMR.* 44:213–223.

69. Linge, J. P., M. Habeck, …, M. Nilges. 2003. ARIA: automated NOE assignment and NMR structure calculation. *Bioinformatics.* 19:315–316.

70. Lemak, A., A. Gutmanas, …, C. H. Arrowsmith. 2011. A novel strategy for NMR resonance assignment and protein structure determination. *J. Biomol. NMR.* 49:27–38.

71. Dockendorff, C., D. M. Gandhi, …, J. T. Sack. 2018. Synthetic analogues of the snail toxin 6-bromo-2-mercaptotryptamine dimer (brmt) reveal that lipid bilayer perturbation does not underlie its modulation of voltage-gated potassium channels. *Biochemistry.* 57:2733–2743.

72. Sack, J. T., and R. W. Aldrich. 2006. Binding of a gating modifier toxin induces intersubunit cooperativity early in the Shaker K channel's activation pathway. *J. Gen. Physiol.* 128:119–132.

73. Kelley, W. P., A. M. Wolters, …, W. F. Gilly. 2003. Characterization of a novel gastropod toxin (6-bromo-2-mercaptotryptamine) that inhibits shaker K channel activity. *J. Biol. Chem.* 278:34934–34942.

74. Sack, J. T., R. W. Aldrich, and W. F. Gilly. 2004. A gastropod toxin selectively slows early transitions in the Shaker K channel's activation pathway. *J. Gen. Physiol.* 123:685–696.

75. Palmer, A. G., III, C. D. Kroenke, and J. P. Loria. 2001. Nuclear magnetic resonance methods for quantifying microsecond-to-millisecond motions in biological macromolecules. *Methods Enzymol.* 339:204–238.

76. Zhao, J., and R. Blunck. 2016. The isolated voltage sensing domain of the Shaker potassium channel forms a voltage-gated cation channel. *eLife.* 5:e18130.

77. Villalba-Galea, C. A., W. Sandtner, …, F. Bezanilla. 2008. S4-based voltage sensors have three major conformations. *Proc. Natl. Acad. Sci. USA.* 105:17600–17607.

78. Infield, D. T., E. E. L. Lee, …, C. A. Ahern. 2018. Replacing voltage sensor arginines with citrulline provides mechanistic insight into charge versus shape. *J. Gen. Physiol.* 150:1017–1024.

79. Ottosson, N. E., M. Silverå Ejneby, …, F. Elinder. 2017. A drug pocket at the lipid bilayer-potassium channel interface. *Sci. Adv.* 3:e1701099.

80. Wood, M. L., J. A. Freites, …, D. J. Tobias. 2017. Atomistic modeling of ion conduction through the voltage-sensing domain of the shaker k^+ ion channel. *J. Phys. Chem. B.* 121:3804–3812.

81. Whicher, J. R., and R. MacKinnon. 2016. Structure of the voltage-gated K^+ channel Eag1 reveals an alternative voltage sensing mechanism. *Science.* 353:664–669.

82. Lee, C. H., and R. MacKinnon. 2017. Structures of the human HCN1 hyperpolarization-activated channel. *Cell.* 168:111–120.e11.

83. Sun, J., and R. MacKinnon. 2017. Cryo-EM structure of a KCNQ1/CaM complex reveals insights into congenital long QT syndrome. *Cell.* 169:1042–1050.e9.

84. Ishida, I. G., G. E. Rangel-Yescas, …, L. D. Islas. 2015. Voltage-dependent gating and gating charge measurements in the Kv1.2 potassium channel. *J. Gen. Physiol.* 145:345–358.

85. Sokolova, O., L. Kolmakova-Partensky, and N. Grigorieff. 2001. Three-dimensional structure of a voltage-gated potassium channel at 2.5 nm resolution. *Structure.* 9:215–220.

86. Columbus, L., J. Lipfert, …, S. A. Lesley. 2009. Mixing and matching detergents for membrane protein NMR structure determination. *J. Am. Chem. Soc.* 131:7320–7326.

87. Poget, S. F., and M. E. Girvin. 2007. Solution NMR of membrane proteins in bilayer mimics: small is beautiful, but sometimes bigger is better. *Biochim. Biophys. Acta.* 1768:3098–3106.

88. Warschawski, D. E., A. A. Arnold, …, I. Marcotte. 2011. Choosing membrane mimetics for NMR structural studies of transmembrane proteins. *Biochim. Biophys. Acta.* 1808:1957–1974.

89. Butterwick, J. A., and R. MacKinnon. 2010. Solution structure and phospholipid interactions of the isolated voltage-sensor domain from KvAP. *J. Mol. Biol.* 403:591–606.

Biophysical Journal, Volume *117*

Supplemental Information

NMR Structural Analysis of Isolated *Shaker* Voltage-Sensing Domain in LPPG Micelles

Hongbo Chen, Junkun Pan, Disha M. Gandhi, Chris Dockendorff, Qiang Cui, Baron Chanda, and Katherine A. Henzler-Wildman

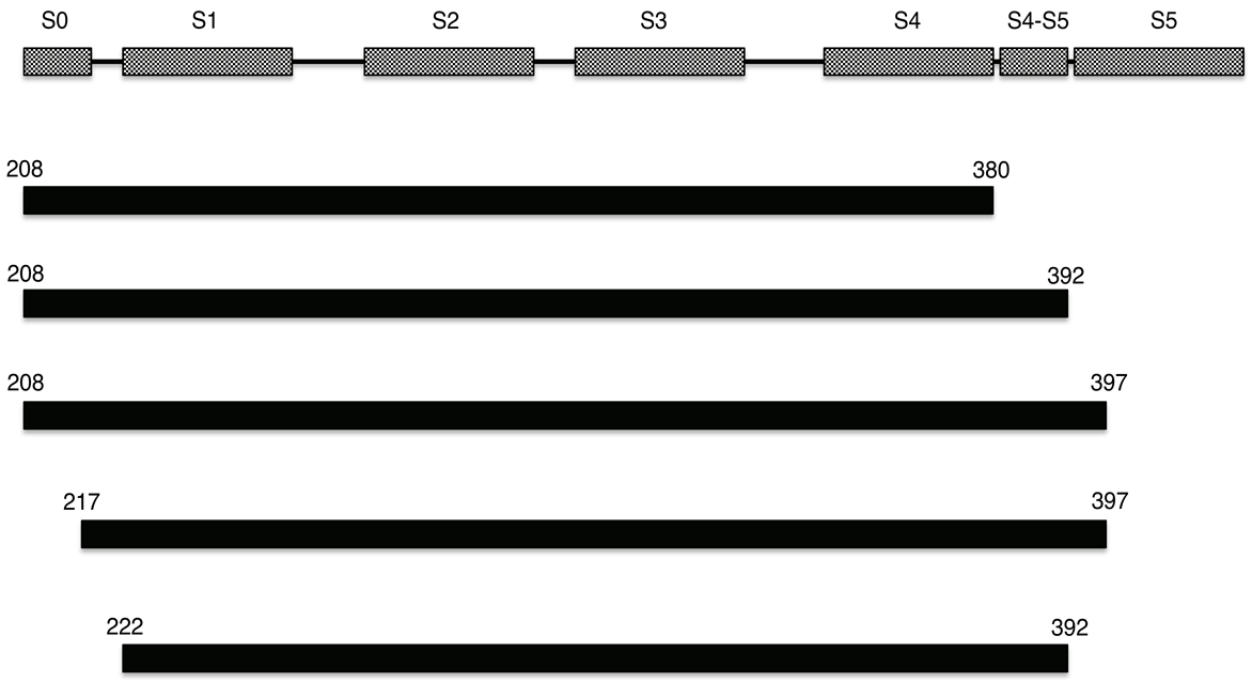

Figure S1. Constructs screened for optimizing Shaker-VSD expression. The highest expressing construct (217-397) was chosen for further NMR studies.

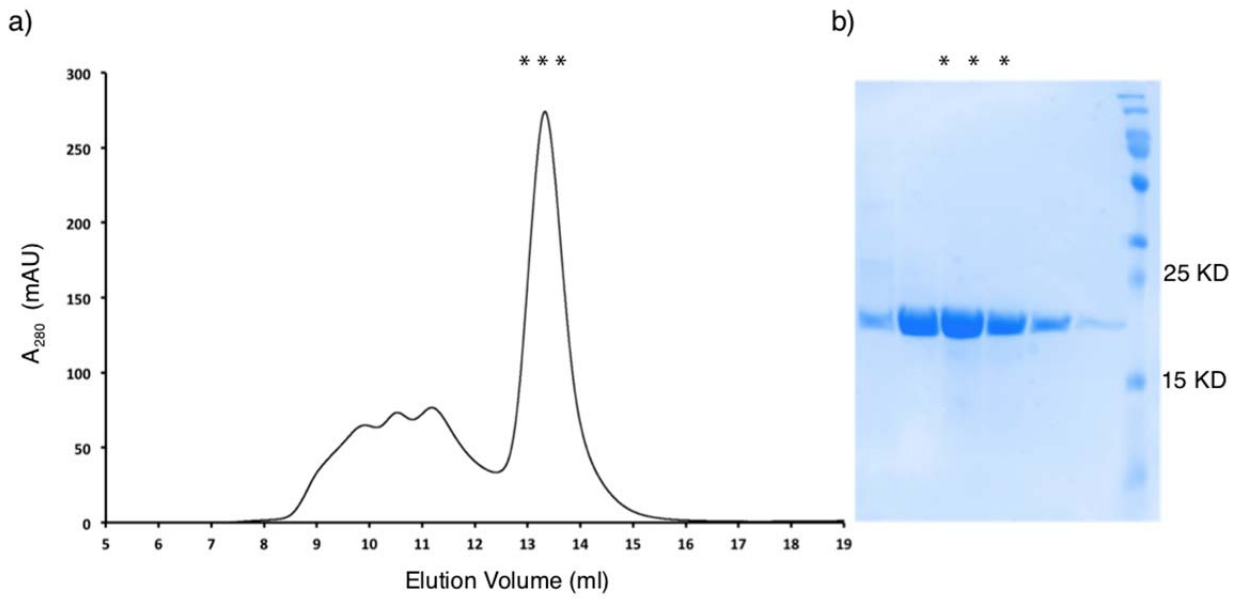

Figure S2. Shaker-VSD purification. (a) Representative gel filtration elution profile of the isolated Shaker-VSD in 0.2% LPPG on a Superdex 200 column. (b) SDS-PAGE gel of fractions from the main peak of the S200 elution profile for the isolated Shaker-VSD shows that the purified protein is a monomer with an apparent molecular mass near 20 kDa as expected.

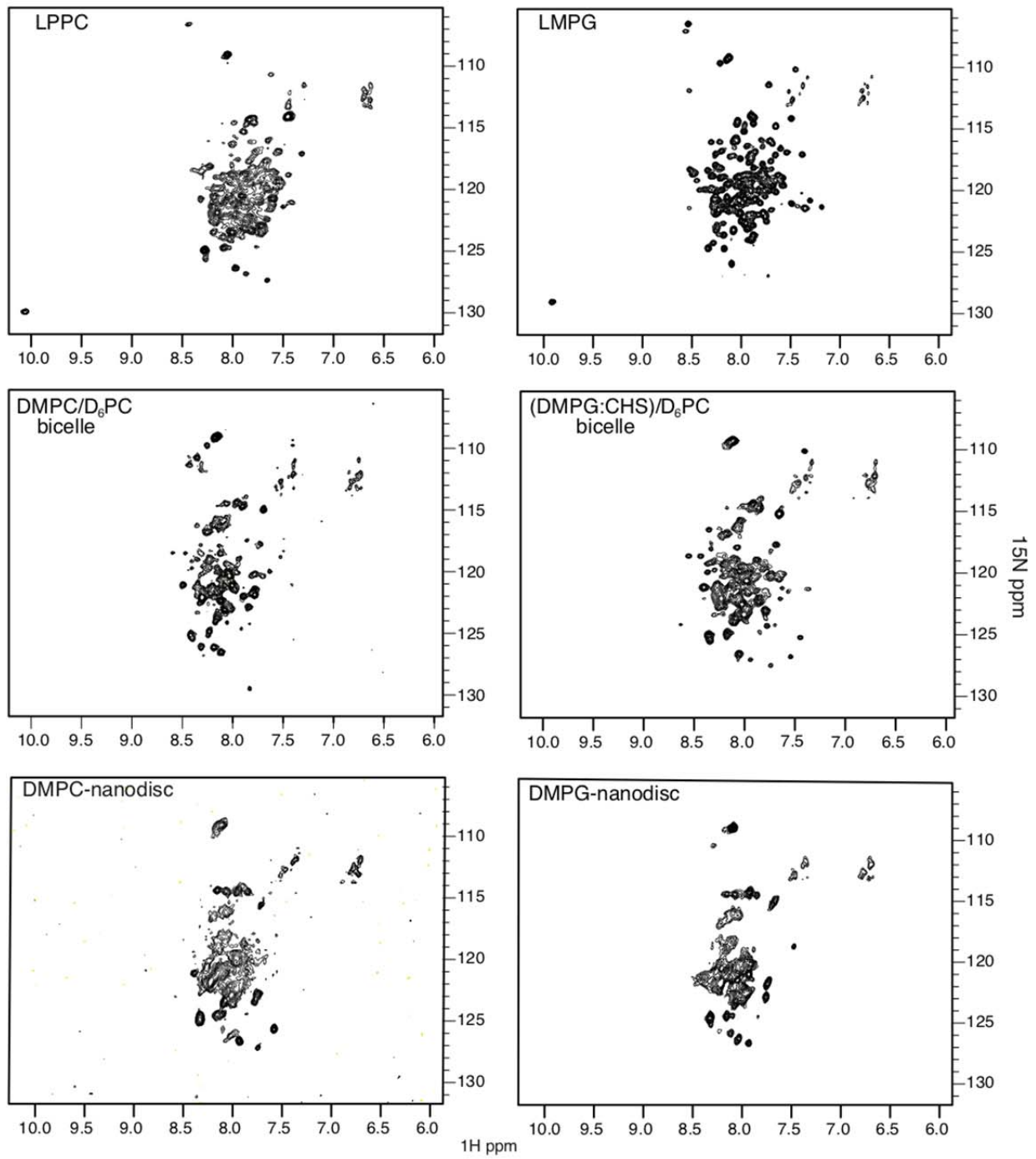

Figure S3. Representative ^{1}H-^{15}N TROSY-HSQC spectra of the isolated Shaker-VSD at pH 7.0 in different membrane mimetics tested during NMR sample optimization. All spectra were acquired on a 750MHz Bruker magnet at 45 °C, except for the DMPC/D_6PC bicelle sample, which was acquired at 37 °C.

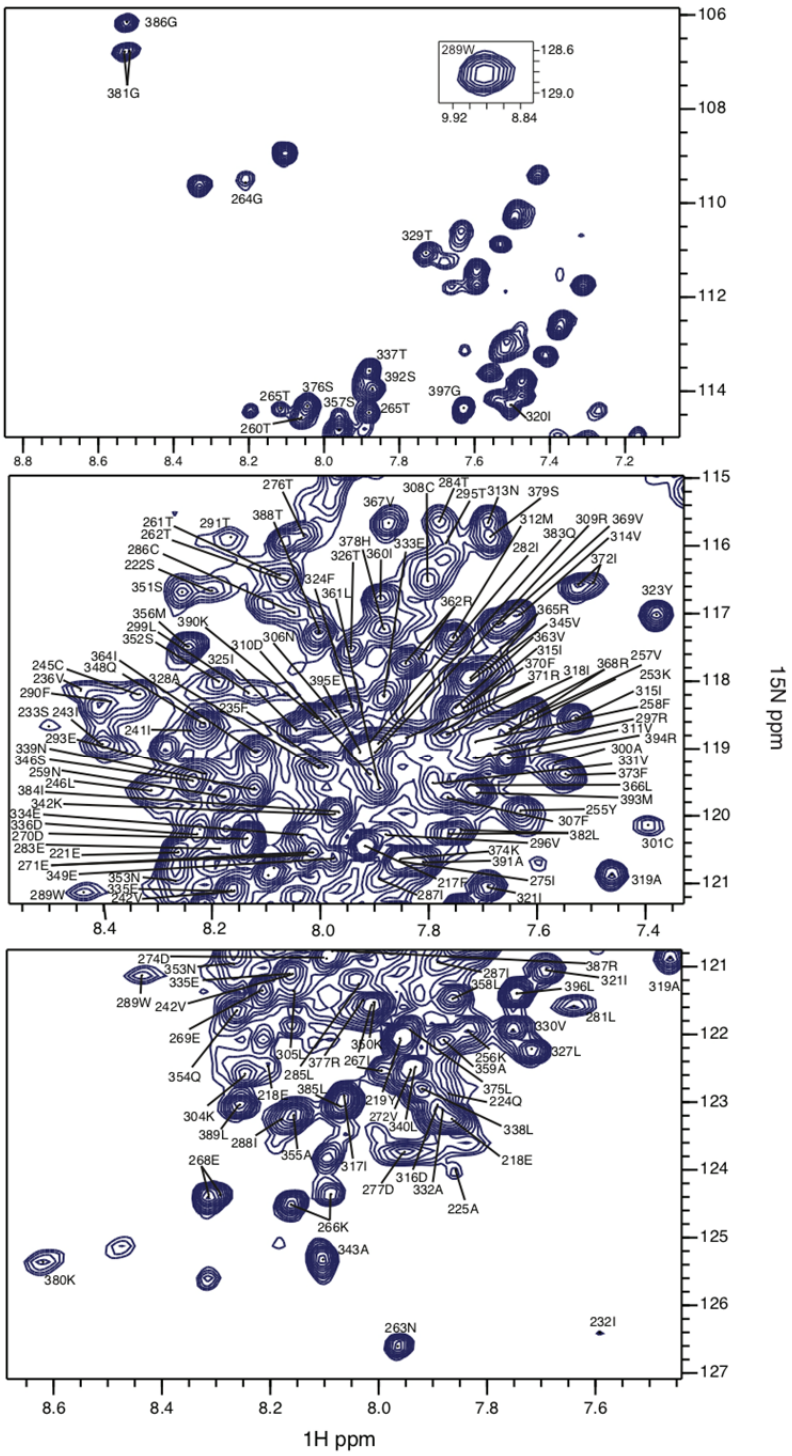

Figure S4. ^{1}H-^{15}N NMR chemical assignments of isolated Shaker-VSD at 45°C in 1.6% LPPG at pH 7.0.

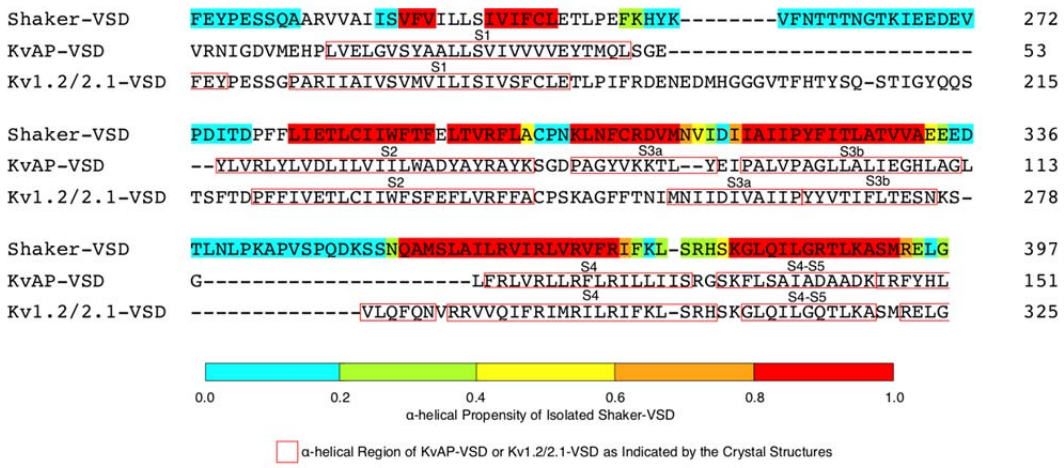

Figure S5. Comparison of secondary structures of isolated Shaker-VSD, KvAP-VSD and Kv1.2/2.1-VSD. The sequence of Shaker-VSD, KvAP-VSD and Kv1.2/2.1-VSD are aligned with Clustal Omega and manually adjusted. The α-helical propensity of isolated Shaker-VSD based on its backbone chemical shifts as shown in Figure 2 is plotted on its sequence with a cyan to red color scale indicating the location of helical regions (0 indicating 0% tendency to form α helix while 1 indicating 100% tendency). Residues in Shaker-VSD without color indicate lack of backbone assignment. Helical regions of KvAP-VSD and Kv1.2/2.1-VSD are marked with red rectangles based on their crystal structures (1ORQ and 2R9R) (1,2). The secondary structural features of isolated Shaker-VSD generally agrees with that of Kv1.2/2.1-VSD, except for S2-S3 linker and S3 transmembrane helix, which is more similar to KvAP-VSD.

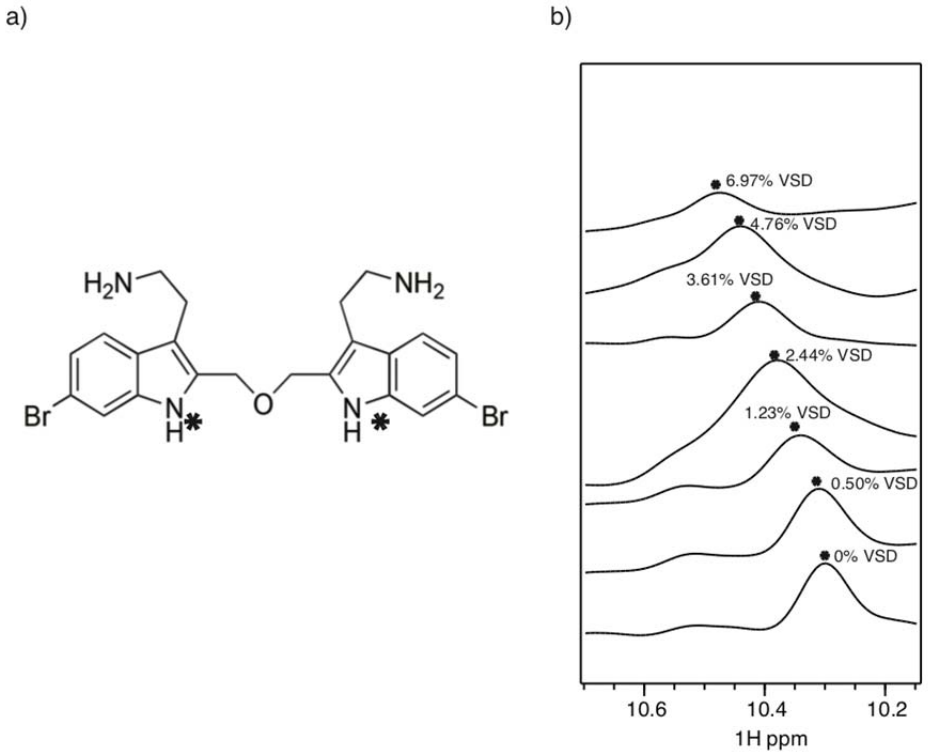

Figure S6: NMR titration of BrET with Shaker-VSD. (a) Structure of BrET with indole marked with *. Stacked plot of 1D ^{1}H NMR spectra of BrET with increasing concentration of added Shaker-VSD in the region of 10ppm. The chemical shift change of the peak corresponding to the BrET indole proton (*) upon Shaker-VSD titration shown in this figure was used to generate the binding curve in Fig. 3.

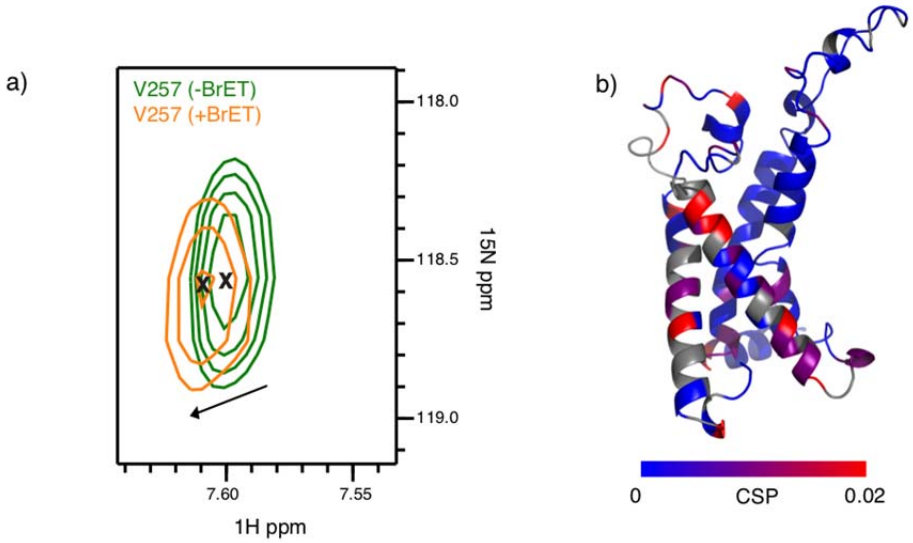

Figure S7. Effect of BrET binding as observed from the NMR spectrum of Shaker-VSD. (a) Overlay of the peak corresponding to Val257 in Shaker-VSD from a TROSY-HNCO spectrum without BrET (green) and with BrET (orange). The chemical shift perturbation is about 0.026. (b) Chemical shift perturbations are plotted on a homology model of isolated Shaker-VSD with a blue to red color scale. Small chemical shift perturbations are observed in many sites across the Shaker-VSD, suggesting that the protein undergoes a global conformational change upon binding.

Figure S8. Residues of Shaker-VSD exhibiting peak doubling in the well-resolved 3D TROSY-HNCO or TROSY-HNCA NMR spectra are highlighted in orange.

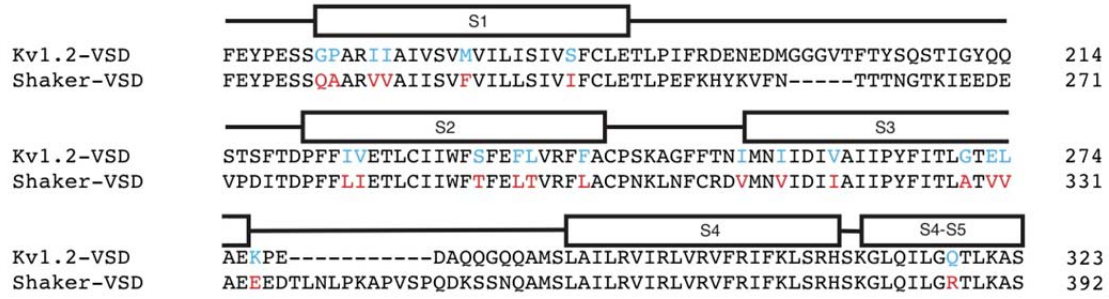

Figure S9: Sequence alignment of Kv1.2-VSD and Shaker-VSD. Residues in the transmembrane helices with different sequence are colored in red and blue.

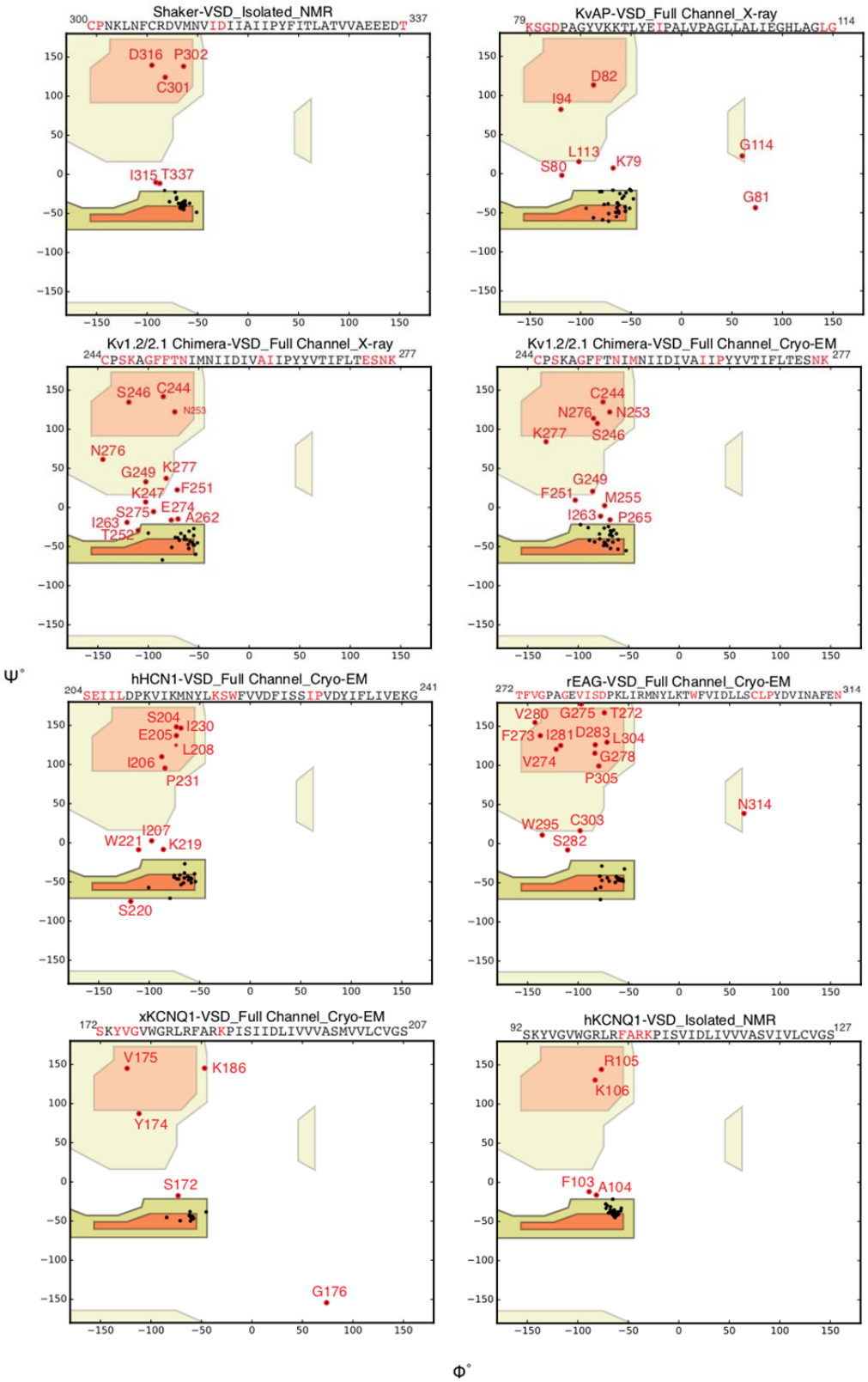
Shaker-VSD_Isolated_NMR
300 CPNKLNFCRDVMNVIDIIAIIPYFITLATVVAEEEDT 337
D316
P302
C301
I315
T337
KvAP-VSD_Full Channel_X-ray
79 KSGDPAGYVKKTLYEIPALVPAGLLALIEGHLAGLG 114
D82
I94
L113
S80
K79
G114
G81
Kv1.2/2.1 Chimera-VSD_Full Channel_X-ray
244 CPSKAGFFTNIMNIIDIVAIIPYYVTIFLTESNK 277
S246
C244
N253
N276
G249
K277
K247
F251
S275
E274
I263
A262
T252
Kv1.2/2.1 Chimera-VSD_Full Channel_Cryo-EM
244 CPSKAGFFTNIMNIIDIVAIIPYYVTIFLTESNK 277
C244
N276
N253
K277
S246
G249
F251
M255
I263
P265
hHCN1-VSD_Full Channel_Cryo-EM
204 SEIILDPKVIKMNYLKSWFVVDFISSIPVDYIFLIVEKG 241
S204
I230
E205
L208
I206
P231
I207
W221
K219
S220
rEAG-VSD_Full Channel_Cryo-EM
272 TFVGPAGEVISDPKLIRMNYLKTWFVIDLLSCLPYDVINAFEN 314
V280
G275
T272
F273
I281
D283
L304
G278
V274
P305
N314
W295
C303
S282
xKCNQ1-VSD_Full Channel_Cryo-EM
172 SKYVGVWGRLRFARKPISIIDLIVVVASMVVLCVGS 207
V175
K186
Y174
S172
G176
hKCNQ1-VSD_Isolated_NMR
92 SKYVGVWGRLRFARKPISVIDLIVVVASVIVLCVGS 127
R105
K106
F103
A104
Ψ°
Φ°

Figure S10: Ramachandran plots of the backbone dihedral angles of the S2-S3 linker and S3 helix in different Kv-VSDs. Backbone φ and ψ angles are extracted from the deposited PDB structures and/or data in the following references: isolated Shaker-VSD (our NMR results); KvAP-VSD in full channel, X-ray (1ORQ) (1); Kv1.2/2.1-VSD in full channel, X-ray (2R9R) (2); Kv1.2/2.1-VSD in full channel, Cryo-EM (6EBK) (3); human KCNQ1-VSD, NMR (calculated with TALOS+ using backbone resonances assignment deposited in BMRB: 19708) (4); *Xenopus laevis* KCNQ1-VSD in full channel, cryo-EM (5VMS) (5); EAG-VSD in full channel, cryo-EM (5K7L) (6); HCN1-VSD in full channel, cryo-EM (5U6O) (7). The ramachandran plot is generated based on theoretical definition of backbone φ and ψ angles in different secondary structural configurations (8), with intense color indicating right-handed helix (orange color indicating favored and yellow indicating allowed regions) and pale orange and pale yellow indicating favored and allowed regions for other secondary structures. Non-helical residues are labeled in red. These analyses were used to define the secondary structure configuration of Shaker-VSD in Figure 5.

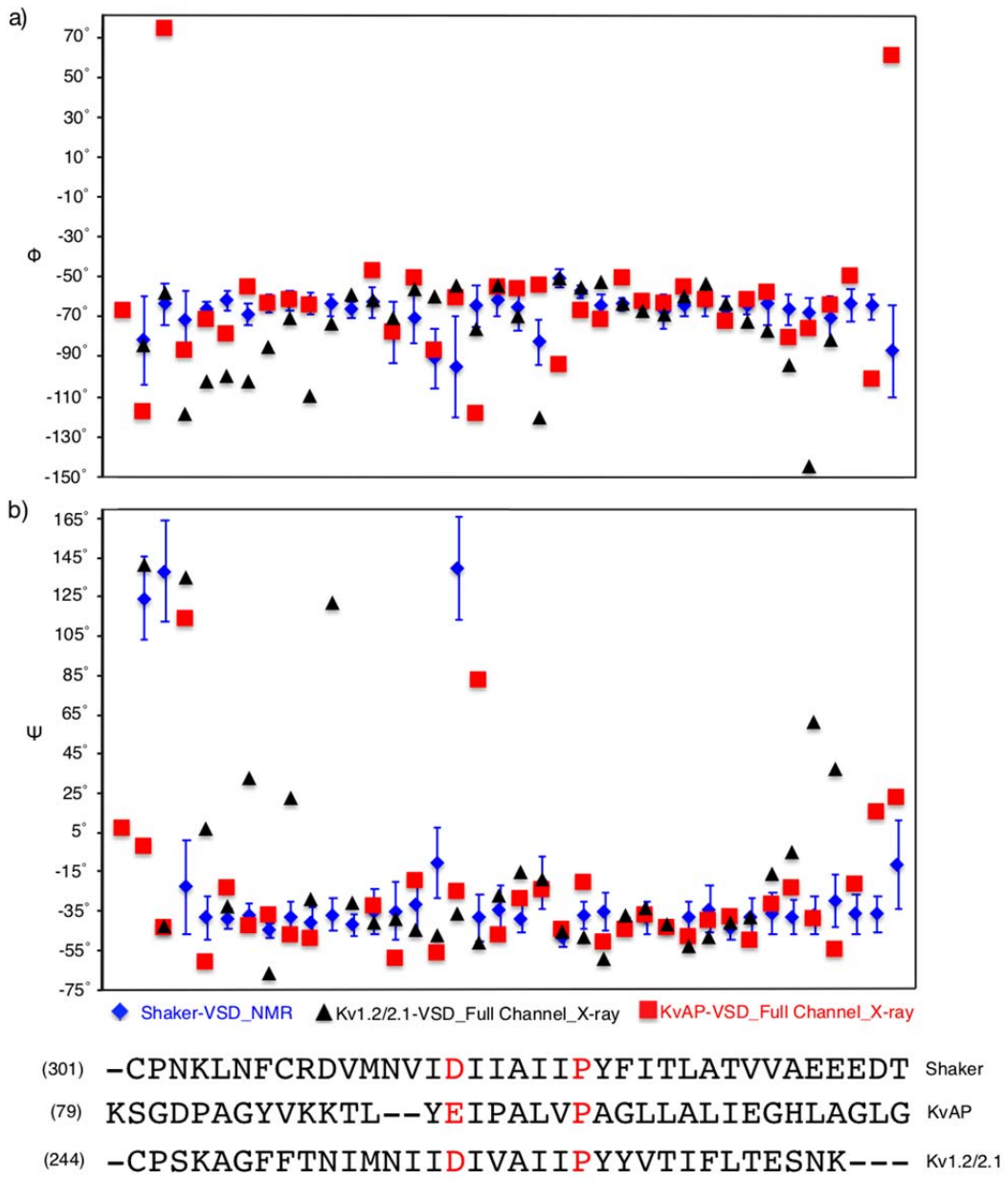

Figure S11: Comparison of backbone dihedral angles of Shaker-VSD, full-lenth KvAP and Kv1.2/2.1 in the S2-S3 linker and S3 helix. Backbone φ and ψ angles are extracted from the deposited PDB structures and/or data in the following references: isolated Shaker-VSD (our NMR results); KvAP-VSD in full channel, X-ray (1ORQ) (1); Kv1.2/2.1-VSD in full channel, X-ray (2R9R) (2). The φ and ψ angles distribution pattern of Shaker-VSD is more similar with that of full-length KvAP crystal structure then that full-length Kv1.2/2.1 crystal structure, indicating that some structural features of this region in Shaker-VSD might be more similar with that of KvAP.

Table S1. Membrane mimetics screened for VSD Reconstitution

Membrane Mimetics			^{15}N-^{1}H HSQC Spectrum Quality
Detergent Micelles	DM		Aggregate
	DDM		Failed to extract from membrane
	OG		Failed to extract from membrane
	CHAPS		Failed to extract from membrane
	Foscholine-12		Poor
	LMPG		Great
	LPPG		Great
	LPPC		OK
	LPPC:LPPG=1:1		OK
	LPPG:Chobimalt=4:1		OK
Bicelles	**Long-chain Lipids**	**Short-chain Lipids**	**^{15}N-^{1}H HSQC Spectrum Quality**
	DMPC	D6PC	Poor
	DMPC:DMPG=3:1	CHAPSO	Reconstitution failed
	POPC:POPG=3:1	D6PC	Poor
	POPC:POPA=3:1	D6PC	Poor
	POPE:POPG=3:1	D6PC	Poor
	DMPC:DMPA=3:1	D6PC	Poor
	DMPG	D6PC	Poor
	DMPG:Cholesterol=9:1	D6PC	OK
	DMPC:DMPA+1%PIP2	D6PC	Poor
	DMPC:DMEPC=3:1	D6PC	Poor
	DMPC:DMTAP=3:1	D6PC	Poor
	DMPG:Cholesterol=9:1	D7PC	OK
	DMPC:DMPA=3:1	D7PC	Poor
	DPPC	D7PC	Poor
	DPPG	D7PC	Poor
	DPPC:Choleterol=9:1	D7PC	Poor
	DPPG:Cholesterol=9:1	D7PC	OK
Nanodiscs	**Lipids**	**Scaffold Protein**	**^{15}N-^{1}H HSQC Spectrum Quality**
	DMPC	MSP1D1ΔH5	Poor
	DMPG	MSP1D1ΔH5	Poor
	DMPC:DMPA=3:1	MSP1D1ΔH5	Poor
Amphipol	A8-35		Poor

Supporting References:

1. Jiang, Y., Lee, A., Chen, J., Ruta, V., Cadene, M., Chait, B. T., and MacKinnon, R. (2003) X-ray structure of a voltage-dependent k+ channel. *Nature* **423**, 33-41
2. Long, S. B., Tao, X., Campbell, E. B., and MacKinnon, R. (2007) Atomic structure of a voltage-dependent k+ channel in a lipid membrane-like environment. *Nature* **450**, 376-382
3. Matthies, D., Bae, C., Toombes, G. E., Fox, T., Bartesaghi, A., Subramaniam, S., and Swartz, K. J. (2018) Single-particle cryo-em structure of a voltage-activated potassium channel in lipid nanodiscs. *Elife* **7**
4. Peng, D., Kim, J. H., Kroncke, B. M., Law, C. L., Xia, Y., Droege, K. D., Van Horn, W. D., Vanoye, C. G., and Sanders, C. R. (2014) Purification and structural study of the voltage-sensor domain of the human kcnq1 potassium ion channel. *Biochemistry* **53**, 2032-2042
5. Sun, J., and MacKinnon, R. (2017) Cryo-em structure of a kcnq1/cam complex reveals insights into congenital long qt syndrome. *Cell* **169**, 1042-1050 e1049
6. Whicher, J. R., and MacKinnon, R. (2016) Structure of the voltage-gated k(+) channel eag1 reveals an alternative voltage sensing mechanism. *Science* **353**, 664-669
7. Lee, C. H., and MacKinnon, R. (2017) Structures of the human hcn1 hyperpolarization-activated channel. *Cell* **168**, 111-120 e111
8. Ramachandran, G. N., Ramakrishnan, C., and Sasisekharan, V. (1963) Stereochemistry of polypeptide chain configurations. *J Mol Biol* **7**, 95-99